Graphene Quantum Dots Embedded MOF-199 Coated with Biodegradable Polymer for Wound Healing Application

By:

Umar Farooq Shah

(Registration number: 00000364691)

Department of Materials Engineering

School of Chemical and Materials Engineering

National University of Sciences & Technology (NUST)

Islamabad, Pakistan

(2024)

Graphene Quantum Dots Embedded MOF-199 Coated with Biodegradable Polymer for Wound Healing Application

By:

Umar Farooq Shah

(Registration number: 00000364691)

A thesis submitted to the National University of Sciences and Technology, Islamabad,

in partial fulfillment of the requirements for the degree of

Master of Science in
Nanoscience and Engineering

Supervisor: Dr. Zakir Hussain

School of Chemical and Materials Engineering (SCME)

National University of Science and Technology (NUST),

H-12, Islamabad, Pakistan

(2024)

THESIS ACCEPTANCE CERTIFICATE

Certified that final copy of MS thesis written by Mr **Umar Farooq Shah** (Registration No 00000364691), of School of Chemical & Materials Engineering (SCME) has been vetted by undersigned, found complete in all respects as per NUST Statues/Regulations, is free of plagiarism, errors, and mistakes and is accepted as partial fulfillment for award of MS degree. It is further certified that necessary amendments as pointed out by GEC members of the scholar have also been incorporated in the said thesis.
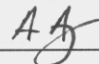
Signature: _____

Name of Supervisor: **Dr Zakir Hussain** _____

Date: 22/5/2024

Signature (HOD): _____

Date: 23/5/24

Signature (Dean/Principal): _____

Date: 23.5-2024

TH - 1

National University of Sciences & Technology (NUST)

MASTER'S THESIS WORK

Formulation of Guidance and Examination Committee (GEC)

ame: <u>Umar Farooq Shah</u>   NUST Reg No: <u>00000364691</u>

epartment: <u>Department of Materials Engineering</u> Specialization: <u>Master of Science in Nanoscience & Engineering</u>

edit Hour Completed: <u>24.0</u>   CGPA: <u>3.69</u>

Course Work Completed

S/No:	Code:	Title:	Core/Elective:	CH:	Grade:
1.	NSE-813	Essentials of Nanoscience and Engineering	Compulsory	3.0	A
2.	MSE-854	Characterization Of Materials	Compulsory	3.0	B+
3.	RM-898	Research Methodology	Additional	2.0	Q
4.	NSE-845	Nanolithography And Device Fabrication	Elective	3.0	B+
5.	MSE-856	Nano Material and Processing	Compulsory	3.0	B+
5.	NSE-812	Environmental Nanotechnology	Elective	3.0	A
7.	MSE-952	Materials For Biomedical Applications	Elective	3.0	B+
3.	ESE-911	Carbon Capture And Utilization	Elective	3.0	A
).	NSE-842	Nano Materials For Energy Applications	Elective	3.0	B+
.0.	IBT-829	Nanobiotechnology: Concepts And Applications	Additional	3.0	B

:e <u>29 - Mar - 2023</u>   Student's Signature

hesis Committee

Jame: <u>Zakir Hussain (Supervisor)</u>   Signature   *Zakir Hussain*
)epartment: <u>Department of Materials Engineering</u>

Jame: <u>Waheed Miran (Internal)</u>   Signature
)epartment: <u>Department of Chemical Engineering</u>

Jame: <u>Shah Rukh Abbas (Internal)</u>   Signature
)epartment: <u>Department of Industrial Biotechnology</u>

e: <u>29 - Mar - 2023</u>   Signature of Head of Department:

APPROVAL

e: <u>29 - Mar - 2023</u>   Signature of Dean/Principal:

School of Chemical & Materials Engineering (SCME) (SCME) H-12 Campus.

National University of Sciences &Technology (NUST)

FORM TH-4

MASTER'S THESIS WORK

We hereby recommend that the dissertation prepared under our supervision by

Regn No & Name: **00000364691 Umar Farooq Shah**

Title: **Graphene Quantum Dots Embedded MOF-199 Coated with Biodegradable Polymer for Wound Healing Application.**

Presented on: **16 May 2024**   at: **1430 hrs in SCME Seminar Hall**

Be accepted in partial fulfillment of the requirements for the award of Masters of Science degree in **Nanoscience & Engineering.**

Guidance & Examination Committee Members

Name: **Dr Shah Rukh Abbas** (ASAB)   Signature: _____

Name: **Dr Waheed Miran**   Signature: _____

Supervisor's Name: **Dr Zakir Hussain**   Signature: _____

Dated: 16/5/2024

Head of Department
Date 17/5/24

Dean/Principal
Date 17-5-2024

School of Chemical &Materials Engineering (SCME)

AUTHOR'S DECLARATION

I Umar Farooq Shah hereby state that my MS thesis titled "Graphene Quantum Dots Embedded MOF-199 Coated with Biodegradable Polymer for Wound Healing Application" is my own work and has not been submitted previously by me for taking any degree from National University of Sciences and Technology, Islamabad or anywhere else in the country/ world.

At any time if my statement is found to be incorrect even after I graduate, the university has the right to withdraw my MS degree.

Name of Student: Umar Farooq Shah

Date: 22-05-2024

PLAGIARISM UNDERTAKING

I solemnly declare that research work presented in the thesis titled "Graphene Quantum Dots Embedded MOF-199 Coated with Biodegradable Polymer for Wound Healing Application" is solely my research work with no significant contribution from any other person. Small contribution/ help wherever taken has been duly acknowledged and that complete thesis has been written by me.

I understand the zero tolerance policy of the HEC and National University of Sciences and Technology (NUST), Islamabad towards plagiarism. Therefore, I as an author of the above titled thesis declare that no portion of my thesis has been plagiarized and any material used as reference is properly referred/cited.

I undertake that if I am found guilty of any formal plagiarism in the above titled thesis even after award of MS degree, the University reserves the rights to withdraw/revoke my MS degree and that HEC and NUST, Islamabad has the right to publish my name on the HEC/University website on which names of students are placed who submitted plagiarized thesis.

Student Signature: _____

Name: Umar Farooq Shah

DEDICATION

"By the grace of Almighty Allah, who is the most Compassionate and Merciful. With heartfelt dedication, I offer this achievement to my Parents, whose unwavering love and support have fortified my journey. To my exceptional supervisor, Dr. Zakir Hussain, your invaluable guidance has illuminated my path. To my esteemed lab mates, your camaraderie and shared endeavors have enriched this journey. This accomplishment stands as a testament to the collective contributions of everyone, inspiring me to continually strive for excellence."

ACKNOWLEDGEMENTS

TABLE OF CONTENTS

REFERENCES 55

LIST OF TABLES

LIST OF FIGURES

LIST OF SYMBOLS AND ABBREVIATIONS

MOF   Metal-Organic Framework

IBU   Ibuprofen

GQD   Graphene Quantum Dots

CQDs   Carbon Quantum Dots

CD   Carbon Dots

CS   Chitosan

T   Temperature

CUS   Coordinatively Unsaturated Sites

NAP   Naproxen

CMS   Carboxymethyl starch

GIT   Gastrointestinal

OCMC   O-Carboxymethyl Chitosan

PVA   (Poly-Venyl) Alcohol

DI   De-ionized

XRD   X-Ray Diffraction

SEM   Scanning Electron Microscopy

FTIR   Fourier Transform Infra Red

UV   Ultra Violet

PL   Photo luminescence

PBS   Phosphate Buffer Saline

ABSTRACT

Globally chronic wounds are substantial health and economic concerns for patients due to the difficulties in wound prolonged healing and increasing cost of wound management. In the following research, we designed and characterized multi-functional co-polymer material, synthesized from safe, non-toxic, biocompatible, and eco-friendly materials. The biodegradable system was effectively synthesized with the help of chitosan, MOF-199, and graphene quantum dots, to deliver water insoluble, ant-inflammatory ibuprofen as a model drug, without using external chemical reagents. The pre-synthesized graphene quantum dots were made from naturally occurring L-glutamic acid, and were imbedded into the MOF-199, synergistically increasing the ibuprofen loading efficiency to 58.3% from 41.8% due to increase in pore surface area and presence of amine functional group of graphene quantum dots electrostatically bonding with ibuprofen hydroxyl groups. The release of the ibuprofen was conducted in simulated body fluid in PBS buffer solution (pH 7.4) at 37 ^{o}C at different interval for 72 hours, where we achieved a control and steady drug release on to the simulated fluid by coating the MOF-199/GQD composite with chitosan causing capping effect and increasing the unloading time of the drug delivery system, total 50.97% of the drug was released in 72 hours for chitosan@IBU@GQD@MOF-199 system. The characterization techniques we used in the above research were SEM, XRD, FTIR and zeta potential analysis, that proved the successful synthesis of chitosan@IBU@GQD@MOF-199, the smooth surface morphology, the interaction between ibuprofen, graphene quantum dots, MOF-199, and chitosan functional groups, and structural stability of MOF-199 while forming polymer composite with chitosan, graphene quantum dots and loading of ibuprofen. By using GQD@MOF-199 composite the drug loading amount increased, enhancing the overall dosage of the pain killer for wound healing and hence the prepared product could be an important candidate in the field of medical care products, especially wound healing application that require large amount of dosage for long durations, which can be achieved through control drug release.

Keywords: Porous structures, Metal Organic Frameworks, MOF-199, Graphene, Quantum Dots, Biodegradable Polymer, Chitosan, Drug Loading, Drug unloading, Wound dressings.

CHAPTER 1:   INTRODUCTION

1.1   Background

Wound healing is one of the important tissue regeneration processes that takes place on the skin punctured, torn, or cut through external factor or stimuli, causing acute or chronic wounds depending upon the damage that has been done. There are several steps that are part of the wound healing process for restoring structural integrity of the skin, which are as follows: Tissue regeneration, granulation, proliferation, and formation [1], [2].

There are two types of wounds: chronic and acute wounds. Acute wounds are known as body wounds caused due to any trauma resulting in tissue loss or any kind of damage to the skin due to external blow that generally heals within three weeks of time frame [3]. Chronic wounds take more than three months to heal, and in the meantime, further complications may occur, for example, a bacterial infection or difficulty in wound healing[4]. There are various types of chronic and acute wounds that can occur due to penetration, impact, burns and blows, which causes complications that are for long durations, resulting an increase in the chances of death or morbidity.

Ulcers mainly due to diabetes, stress, or caused in vascular regions are common example of chronic wounds[5]. For example, pain in the diabetic patient chronic wound usually comes from, chronic inflammation, incomplete angiogenesis, collagen metabolism not working properly, and several other factors[6]. All these reasons make healing the process of the diabetic wound a difficult process. (In the United States around 4 million people are diagnosed of chronic wounds. Specifically, 40-60% of the chronic wounds patients in the United States are affected with diabetic foot ulcer, costing almost 1 billion dollars, paid by the insurance companies, health care providers and patients[7-9] . Different types of medical procedures have been used including, tissue engineering products, autografts, and wound dressings, but none of the conventional methods are effective in healing chronic wounds[10]. There is a huge gap between the number of chronic wounds

infection incidents occurring and limitation of the wound healing procedures available, it is the need of the hour to develop novel practices and material systems that would overcome unmet medical challenges in wound care management[11], [12].

1.2   Wound Healing and Treatment Mechanisms

The process of wound healing is carried out in several steps, and if any stage is affected it can cause a severe dysfunction. If the inflammation lasts for several months or years resulting in an increase in healing time would classify the wound as chronic which may result in different pathological activities, including wound infection or increased protease activity[13]. Normally, the acute wounds can take up to 3 weeks to heal, while for chronic wounds the healing period might be greater than 3 months[14]. The chronic wound results from the damaging of all the skin layers simultaneously. (The major reason for the chronic wound are the complications caused by other diseases, such a foot ulcers caused by diabetes, spinal cord injuries causing pressure sore or neurodegenerative diseases[1]

1.2.1   Homeostasis
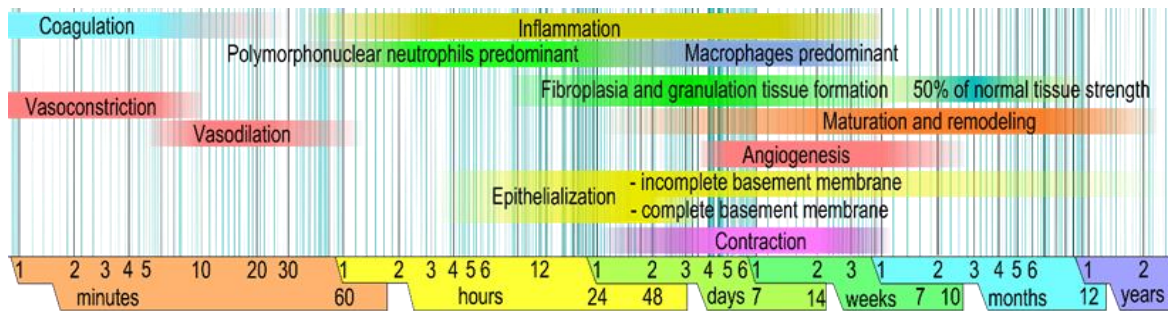
Figure 1.1: Continuous wound healing stages starting from homeostasis followed by inflammation to cell proliferation, and remodeling.

There are four continuous stages in the process of wound healing **(fig.1.1)**, which starts from homeostasis followed by inflammation, to cell proliferation and remodeling. All of the mentioned processes is a combination of different interactions between cells, factors related to coagulation, connective tissue, factor related to growth, cytokines, and

2

the vascular system [1], [2]. When the skin tissue gets injured, bleeding may occur due to which vasoconstriction happens to restrict the blood flow [3]. The coagulation process starts as the aggregation occurs in the wound, (forming a fibrin mesh that causes the wound to harden. The affected site produces extracellular matrix (ECM) which releases procoagulants that facilitates the formation of thrombi [4], [5].

1.2.2   Inflammation

The second stage of wound healing process include inflammation, in which neutrophils, macrophage and lymphocytes traves to the wound, causing an inflammatory response, for almost 3 weeks [6]. Prostaglandin and histamine gets released that results in the vasodilation increasing the permeability of the blood vessels in the surroundings, that directly supports the inflammatory response. After controlling the blood flow, as the wound formation takes the neutrophils are sent to the surrounding blood vessels that are affected, in order to kill all the unwanted external organism through phagocytosis [7]. Macrophages also helps neutrophils to remove dead or damaged cells, in tissue restoration, and defense mechanism [8]. Cytokines and chemokines are released by activating immune cells, such as Langerhans, mast, and gamma-delta (c-d) cells. Mastocytes and leukocytes also contribute to the further development of wound healing [1].

1.2.3   Proliferation

When inflammatory phase finishes, cell proliferation phase begins, resulting in the new tissue formation causing, granulation, re-epithelialization, and the restoration of new vascular networks [9]. Epidermal barriers are repaired with the help of keratinocytes. In parallel, ECM and angiogenesis forms due to endothelial cells and fibroblast, coagulating macrophages and generating different growth factors at the wound site such as tumor necrosis factor (TNF) and transforming growth factor (TGF) [10], [11]. Granulation tissue that is reddish in color indicates wound healing, and the tissue turns black when any kind of infection occurs.

The epithelial cells in the moist environment during the last stages of epithelialization can speed up the wound healing and migration process [12], [13].

1.2.4   Re-modelling

Remodeling, the final phase of wound healing, involves the contraction and restructuring of the newly created matrix. It lasts for several years and begins in the third week following the creation of the wound. Its primary objectives are restoring healthy structural tissue and enhancing tensile strength, including: the remodeling of granulation tissue to produce scar tissues[14];the breakdown of type III collagen and the increase of type I collagen; wound closure; the reduction of cells and the rise in collagen fiber level [1] [12], [15].

1.2.5   Conventional Methods

One of the many biological processes in the human body is the regrowth and regeneration of cutaneous tissue. Promising results have been gained from a range of techniques that have been examined in order to achieve healthy skin and an effective wound healing process. Both modern and traditional therapy can be used to heal wounds. Using special natural compounds from plants, honey, propolis, and larvae were among the traditional approaches. All across the world, including Asia, Africa, and Latin America, uses these natural remedies. Using leech therapy to remove unnecessary skin and tissue to aid in wound healing is a very realistic example of an alternate traditional procedure [16]. Natural sugars like honey are useful for treating a variety of wounds externally and are essential for the re-epithelialization of wounds [17]. Conversely, some plant-derived extracts, such those in calendula officinalis and aloe vera, can aid in promoting wound healing and skin regeneration when applied topically [18], [19]. Currently, debridement, ischemia, infection, medicinal nutrition, etc. are among the fundamental requirements of chronic wound care. [20].

Apart from conventional therapies, there exist other modern approaches for wound healing. One of the newest techniques for healing wounds in clinical practice is hyperbaric oxygen therapy as shown in **fig.1.2**, which works to treat difficult or complicated ulcers by increasing oxygen flow to the effected regions and preventing amputation [21], [22].
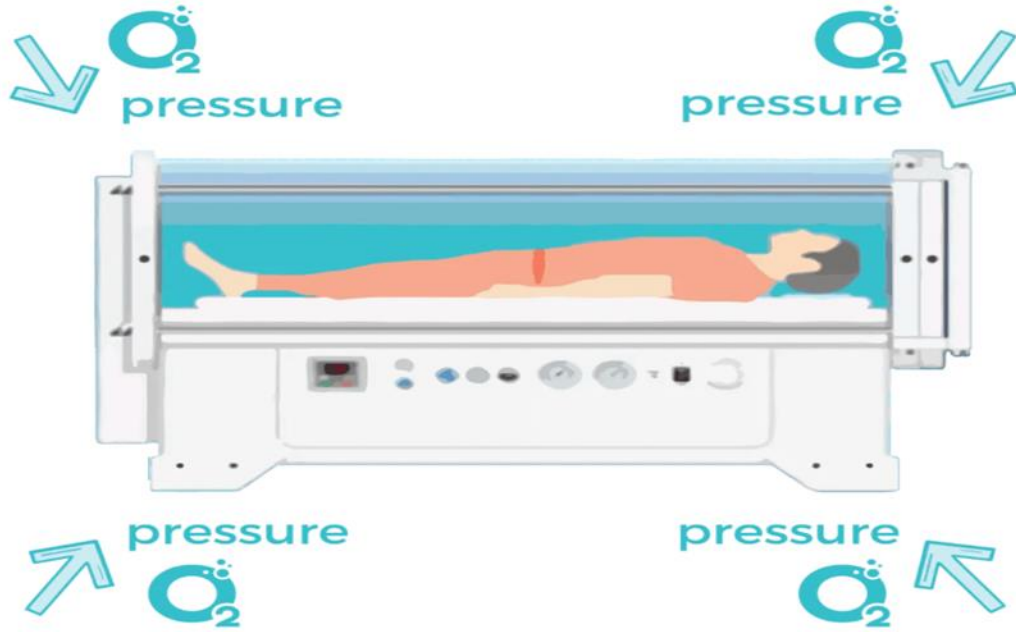
Figure 2.2: Hyperbaric Oxygen Therapy Chamber.

Negative pressure therapy, when used to treat postoperative wound issues, involves accelerating the healing process by reducing edema, changing capillary perfusion, and increasing collagen production and angiogenesis. In therapeutic settings, several wound dressings are used to maintain the moisture content of the wound. All of these dressings promote wound healing, prevent infection, and protect the wound base. Today's most popular materials for wound dressings are collagen, chitosan (CS), silica gel, and hyaluronic acid (HA) [10]. Heparin, gelatin, cellulose, alginate (Alg), and other biomaterials are also included in the conventional materials [24]. Applying dressings composed of polymers that mimic the chemical and physical properties of the tissue speeds up the healing process of wounds [29].

1.3   Advance Materials for Biomedical Applications.

The process of wound healing is dynamic and complex, requiring precise synchronization between various cell types in the right extracellular matrix. The four overlapping phases of the wound healing process involves hemostasis, inflammation, proliferation, and maturation, are carefully controlled. All four stages must occur in a timely and in a sequential manner for wound healing to be effective. A number of variables

may disrupt one or more of these stages of the healing process, leading to incorrect or compromised wound healing and chronic wounds that do not heal. The need for the creation of fresh and innovative treatment is due to the limitations of traditional wound therapies, as well as the difficulties associated with chronic non-healing wounds. Through the interaction of nanomaterials during various stages of wound healing, nanotechnology offers novel and alternate ways to speed up the healing of chronic wounds.

1.3.1   Porous Materials

Made of organic linkers and inorganic metal ions, metal organic frameworks (MOFs) are a novel form of crystalline, porous coordination polymer material. Because of their important uses in the biomedical sector, metal organic frameworks, a novel type of porous material, have drawn a lot of attention from researchers in recent years. Metal organic framework is ideal for loading because of its appealing qualities, including ultra-high porosity, wide surface area, excellent thermal stability, and simple synthesis makes it suitable for loading purposes. Because MOFs are easily functionalized, they can be used in biomedical applications. Additionally, because of their variable pore size, a wide range of medicinal medicines can easily wrap around them [23].

1.3.2   Graphene Quantum Dots

Graphene quantum dots and quantum scale carbon materials, also known as carbon quantum dots (CQDs) or carbon dots (CDs), are young members of the carbon nanomaterial family [24], [25]. After Xu et al.'s unintentional discovery of these tiny (less than 10 nm) carbogenic fluorescent nanoparticles in 2004, a whole new field of nanoparticle research with a broad variety of applications was opened [26]. Generally speaking, carbon, oxygen, and hydrogen are abundant in CDs. By using the right techniques, several additional elements, as per requirement of the application, such as nitrogen, sulphur, boron, etc., can be doped to change the characteristics [27]. Moreover, CDs have adjustable fluorescence and strong water solubility. Generally speaking, CD's high water solubility is a result of the carboxyl functionality that covers their surface. However, it is simple to change the physical characteristics, lessen toxicity, and change the

fluorescence behavior of CDs by functionalizing them with different chemical groups and passivating their surface [25], [27]. Additionally, CDs are highly biocompatible, have good photostability, and are simply and affordably manufactured, all of which enable their numerous uses in the fields of drug administration, optoelectronics, bioimaging, photocatalysis, and biosensors [24], [28], [29].

1.3.3 Chitosan

In nature, chitin is often found in organisms including mushrooms, insects, and crustaceans. As a deacetylated derivative of chitin, chitosan can be chemically synthesized with varying degrees of deacetylation. Chitosan is a linear polysaccharide made up of either deacetylated or acetylated D-glucosamine linked by β-(1-4)-linkage. It is biocompatible, biodegradable, and non-toxic. As a result, it has been used in many different industries, including food additives, cosmetics, water purification, agriculture, medication delivery systems, and tissue regeneration. Some additional properties of chitosan include immunological stimulation, anti-fungal, anti-bacterial, and anti-inflammatory properties. Chitosan is a great biomaterial for the creation of novel medications and medical devices because of its adaptability and versatility [30], [31], [32].

CHAPTER 2: LITERATURE REVIEW

2.1   Metal Organic Frameworks

Porous materials are divided into different classes, these classes consist of three main categories, the microporous zeolites, mesoporous silica and metal oxides, and macro porous polymer structures. According to IUPAC, these classifications are basically done on the basis of the pore size, if the pore size is between 0-2 nm than the material is classified as mesoporous, if the pore size of a material is less than 50 nm than its classified as microporous, and if the pore size is greater than 50 nm than its categorized as macroporous. Due to their unique characteristics and small pore size, they are preferred choices in different industries including, energy sector, for catalysis, adsorption, ion-exchange and host guest assembly. [33].

Generally, the porous materials were either synthesized from organic or inorganic materials. Inorganic porous materials, silica or metal oxides are crystalline in nature, because these types of porous materials are fully inorganic, they suffer from structural flexibility, functional tailorability and mechanical strength, on the other side porous materials made up of polymer are amorphous or partially order in ploy-crystalline forms such as diamond or graphite [34]. A new class of materials has been introduced, known as organic-inorganic hybrid porous materials, that combines the beneficial properties of both the classes and may show exceptional characteristics as compared to the individual properties of both the classes [35] .

As an emerging microporous, coordinating polymer, inorganic-organic material, Metal organic frameworks (MOFs) have recently got attention as a class of organic–inorganic hybrid materials for variety of applications [36].

MOFs are both crystalline and porous materials made up of metal ions/ ligands, connected through an array of organic linkers as shown in **fig. 2.1.** A significant characteristic of MOFs is that its structure, pore size, and functionality, according to

literature, can be finely controlled by the selection of metal and the organic linker as building blocks, and how they are connected to each other. [37][21-23].
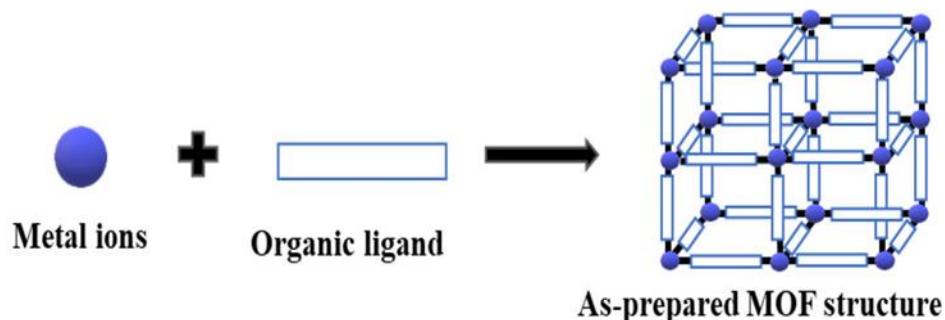
Figure 2.1: Formation of MOF structure by formation of chemical bonds between the metal ions as nodes and the organic molecule as a linker [54].

2.1.1 Synthesis of MOF

Numerous distinct MOFs have been synthesized thanks to the great diversity of inorganic and organic components. Presently, the category of MOF material is comprised of around 20,000 distinct structures, as documented in the Cambridge structure database and examined during the last two decades [41].

Typically, solvothermal conditions (i.e., 100 ºC < T < 250 ºC) or room temperature are used to synthesize MOF crystals **(figure 2.2).** For a typical solvothermal recipe, all reactants (metal salts, ligands, and solvents) are added in one step to sealed vessels, and then the temperature is heated just below subcritical conditions for a few minutes, hours, or days, depending on the type of MOF.

The temperature is the primary parameter because it sets up the reacting system in a way that maximizes thermodynamically favorable coordination contacts and reactant diffusion, so enabling the spontaneous self-assembly of ordered structures or lattices. Aside from water, the most common solvents include pyridine, alcohols, and dialkyl formamides [38].

Figure 2.2: Conventional solvothermal synthesis procedure.

2.1.2   MOF for Biomedical Applications

Metal organic frameworks have gained the attention of researchers due to their potential applications in many areas, especially for the delivery of bioactive molecules. Due to MOFs high porosity, large surface area, and tunability functionality, they have drawn a lot of attention for biomedical applications, especially to be used as platform for drug delivery [42], [43], [44], [45]. Compared to widely reported porous materials (e.g. silica), the synthetic procedure of MOFs is much simpler and more efficient [46], [47]. Another advantage is that the pore structure of MOFs can be controlled by changing the conditions of reaction or the selection of different metal ions and ligands. Moreover, the functions of MOFs can be altered by simply changing the ions to construct the framework. Compared with conventional nanocarriers (e.g., inorganic zeolites, silica nanomaterials, and organic nanocarriers of lipids/polymers), MOFs possess some unique properties that enable them to perform as promising nanoplatforms for drug delivery and bioimaging. Firstly, MOFs are compositionally and structurally diverse, allowing the facile synthesis of MOFs with different compositions, shapes, sizes, and chemical properties.

Secondly, for drug/probe delivery, a biodegradable nano formula is needed, as the material must transport and release the drug/probe to generate effective results at the intended disease site. MOFs are biodegradable due to the presence of relatively labile metal

ligand bonds; this feature makes it possible to rapidly degrade the composite material and release the loaded drug or probe [44].

One strategy to further enhance MOFs features is their combination with supportive matrices (*e.g.* metal nanoparticles, polymers, and carbon nanotubes) to engineer MOF-composites that will maintain the multifunctional properties of MOFs while mitigating the shortcomings of both components [26–30]. Consequently, the composites resulting from the blend of MOF and other auxiliary components make them suitable for a large range of applications, including controlled drug release *via* cutaneous administration. The delayed or improper healing of wounds is today a global health issue that affects millions of people suffering from cancer and ulcerating diabetic lesions. It has an enormous negative impact not only on the patient's quality of life but also on the world economy, where, in 2006, 30% of the total costs in dermatology were linked to the treatment of wounds. In the United Kingdom alone, an estimated expenditure of £3 billion was registered in 2001, jumping to £5 billion in 2015 [31, 32]. Therefore, the design of novel multifunctional nanocomposites combining wound protection and active disease treatment has higher market value and application prospects in the field of wound care. In this context, there is scope to investigate the application of MOF-composites, and especially the MOF/Polymer composites, to engineer bioactive wound dressings; that is to say, systems capable of effectively aiding the healing process, by the slow release of drugs and active agents to the wound site, while forming a barrier to stop the penetration of bacteria to the wound environment [33, 34]. In fact, MOFs have recently been investigated for their antimicrobial activities, generally attributed to their metallic ions (*e.g.* Cu, Fe, Zn, and Ag) [35].**)**

Li-Li tan et al's Research was conducted on a new theranostic nanoplatform for advanced biomedical applications, which included the construction of carboxylatopillar arene-based supramolecular switches as gating entities and monodisperse zirconium metal-organic frameworks (MOFs) as drug carriers. This allowed for controlled drug release of Fu (fluorouracil) **(fig.2.3)**, which was triggered by bio-friendly Zn^{2+} ions (found in synaptic vesicles) and auxiliary thermal stimulus. Large pore diameters for drug encapsulation, outstanding biodegradability and biocompatibility, incredibly low cytotoxicity and premature drug release, and superior dual-stimuli responsiveness were all

displayed by this on-command drug delivery system. An attractive strategy for the treatment of brain diseases was suggested by Zn [2+] and thermally driven medication release with incredibly minimal premature release. [46].
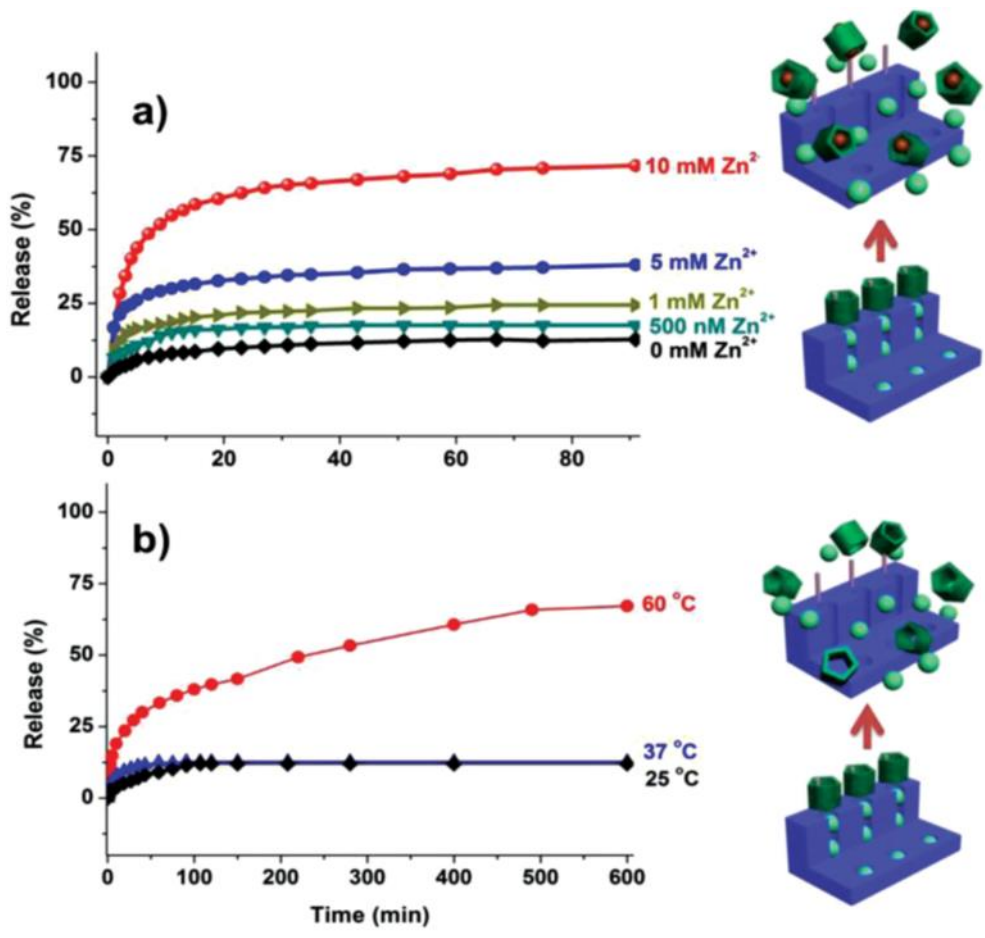
Figure 2.3: Release profile les of the Fu-loaded, CP5-capped UiO-66-NH-Q operated by (a) competitive binding with Zn 2+ and (b) thermal activation [60].

2.2 MOF-199

Since it was one of the first porous MOFs to be found, the Cu-based MOF-199 [Cu3(BTC)2] has served as a reference for research on a number of general MOF properties. The three typical microporous sites (5, 11, and 13.5 Å in diameter) [48], [49], that make up the MOF-199 3D framework structure are copper paddle-wheel construction units coupled by organic linkers made of trimesic acid **(fig.2.4).** There has also been

investigation into this framework as a potential host for the development of bio-oriented guest@MOF composite systems [50], [51], [52] . When MOF-199 is activated at low pressure and moderate heating (100 °C), it creates an exposed Cu^{2+} site structure that is chemically activated. Interestingly, the CUS in MOF-199's pores are very accessible and exhibit robust guest molecule binding sites [53]. Due to its efficient antibacterial and antifungal activity, increased wound healing characteristics (attributed to the Cu ions), and regulated release of several chemotherapeutic drug cargos, MOF-199 has been regarded as a leading platform for biomedical applications [52], [54].
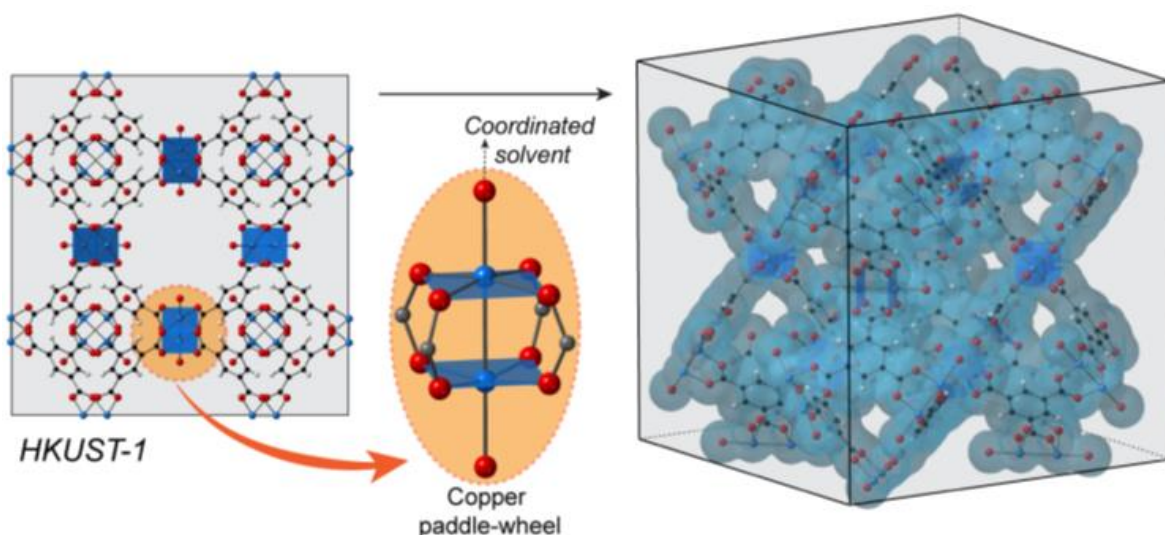
Figure 2.4: Schematic representation of MOF-199 structure.

Xiao j at el's carried out research on folic acid functionalized MOF-199, to study the cytotoxicity and drug delivery rate for efficient wound healing systems. Cu^{2+} is reported to have good angiogenesis stimulation, collagen formation and re-epithelialization properties, but due to their cytotoxicity concerns it can not be used directly. The incorporation of folic acid into MOF-199 enabled the slow release of copper ions, which reduced cytotoxicity and enhanced cell migration in vitro. In vivo, F-MOF-199 induced angiogenesis, promoted collagen deposition and re-epithelialization, and increased wound closure rates. These results demonstrate that folic acid incorporation into MOF-199 NPs is a simple, safe, and promising approach to control Cu^{2+} release, thus enabling the direct application of Cu-MOF NPs to wounds [52].

Chiericatti at el, They used MOF-199 for a novel application of anti-fungal activity in their subsequent study **(fig.2.5).** It was effective to use the MOF-199 metal-organic framework (MOF) as a biocidal material against mold and representative yeast. When it came to Saccharomy cescerevisiae, the growth was entirely suppressed by the synthesized MOF, whereas Geotrichum candidum's growth was lowered from 6.16 to 1.29 CFU mL^{-1}).

The material's crystalline structure gradually broke down, due to the surface extra-framework Cu(I), which led to the release of copper ions into the culture medium and the antifungal effect. This work demonstrates the possibility of releasing biologically active copper ions under control using metal–organic frameworks based on copper [54].
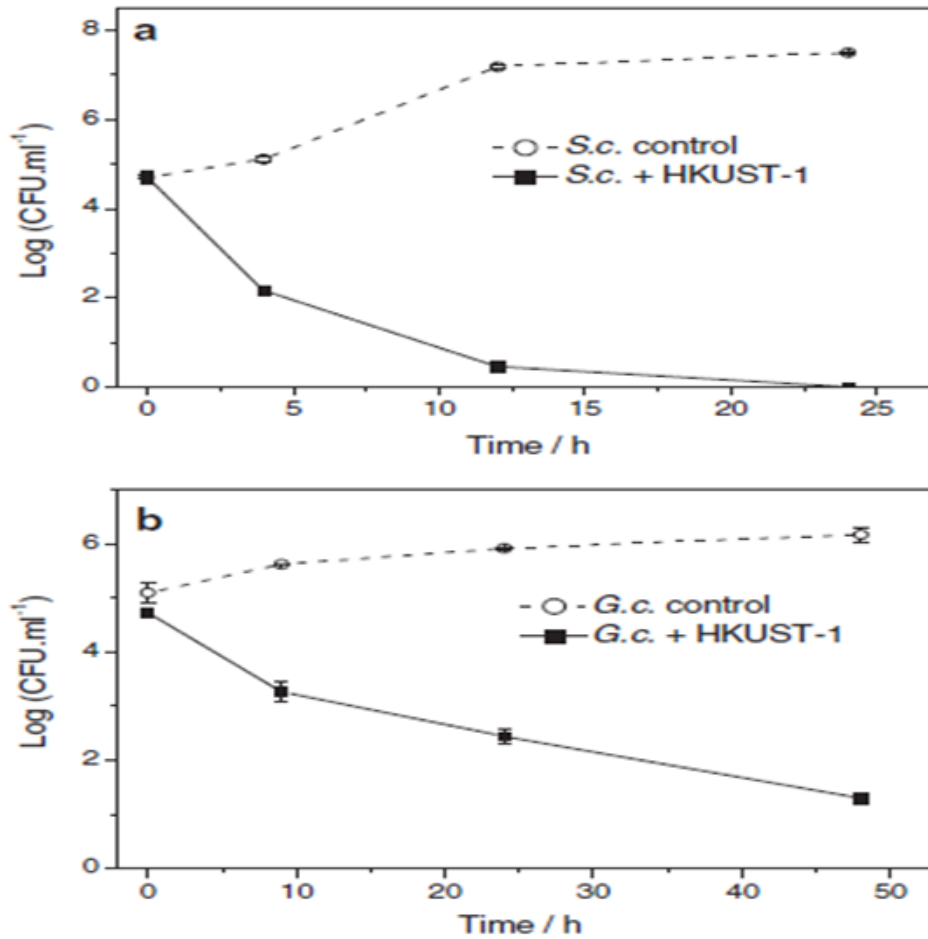
Figure 2.5: Viable colony counting at different times with and without the addition of MOF-199 for: (a) S. cerevisiae; (b) G. candidum [68] .

2.3　MOF Composites

Strong coordination between the metal ions and linkers, which are tunable to support the sensible design and change of the structure, determines the MOF structure itself.

If the MOF pore structure contains CUS sites, then this robust coordination bonding can be extended to the guest molecules. In order to create composite@MOF assemblies, functional "guest" molecules, such as drug molecules, are added to the "host" MOF nanoporous cavities. This process is known as functionalization of the MOF.

2.3.1　Synthesis

The incorporation of guest molecules into the porous MOF structure has been approached from many perspectives. The most popular methods for creating composite@MOF drug-loaded systems are covered in the sections that follow.

These methods may be able to lower some of the current obstacles to using MOFs as drug delivery platforms.

2.3.1.1 Twostep ex-situ encapsulation

Activated MOF particles are submerged in a solution containing the guest molecule to be encapsulated in order to accomplish the ex-situ confinement of foreign molecules in MOF pores **(fig.2.6a).**

Due to its simplicity, versatility in handling a wide range of medicines and functional compounds, and ability to produce a vast array of MOF composite systems, it is undoubtedly the most widely utilized technique [55].

The process includes synthesizing the host metal-organic framework (MOF), activating it to remove coordinating solvent, immersing it in the guest solution to encapsulate it, and then washing and drying it. The parameters on which this process mainly depends on:

- Immersion time

- Solvent dependency

- Choice of appropriate solvent

- Chemical affinity of the molecules used.
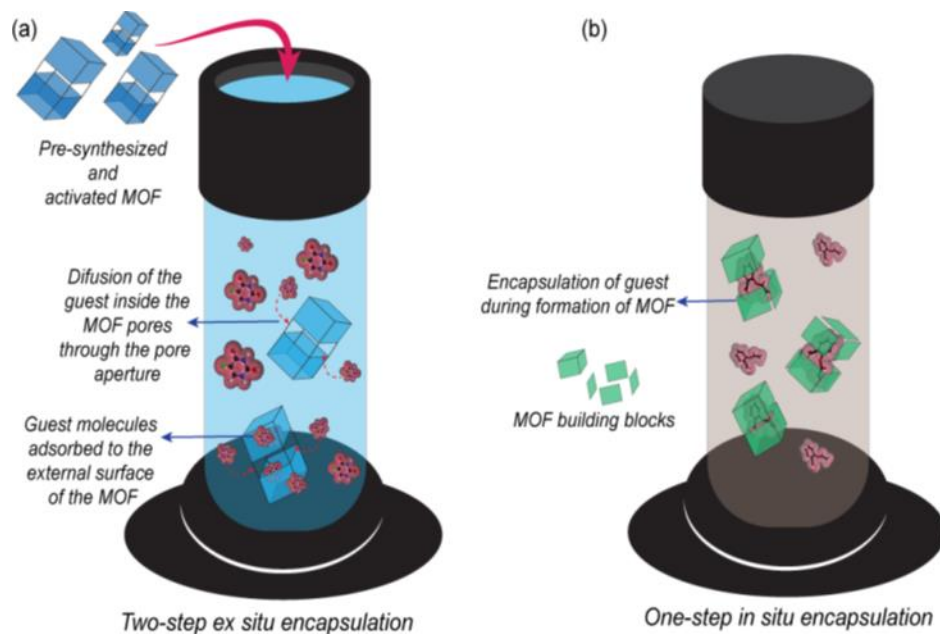
Figure 2.6: Schematic representation of techniques commonly used for guest confinement into the host MOFs. (a) ex situ, (b) in situ encapsulation.

2.3.1.2 One step ex-situ encapsulation

By enabling guest confinement to occur simultaneously with MOF production, the in situ technique eliminates the composite formation caused by post synthetic stages (**fig.2.6b**). Consequently, the drug loading depends only on the guest/pore dimensions and is no longer dependent on the size of the accessible pore aperture. Nonetheless, the guest must stay stable in order for the MOF synthesis to occur, which may restrict the amount of guest MOF combinations that work with this approach. The production of composite@MOF systems can greatly benefit from the one-step encapsulation process, both in terms of the environment and the economy.

Concerning the confinement of guest molecules, the in situ and ex situ encapsulation techniques offer inherent differences in terms of performance, advantages, and disadvantages. To determine the best approach for a given set of targeted applications, these two divergent paths must be thoroughly and methodically examined.

2.3.2 Biomedical Applications

Pooresmai M at el, for the first time in research synthesized in-situ graphene quantum dots embedded bio copper MOF structure loaded with NAP through ex-situ method and coated with carboxymethyl and chitosan for colon specific drug delivery. They were successful in increasing the encapsulation efficiency of bio copper
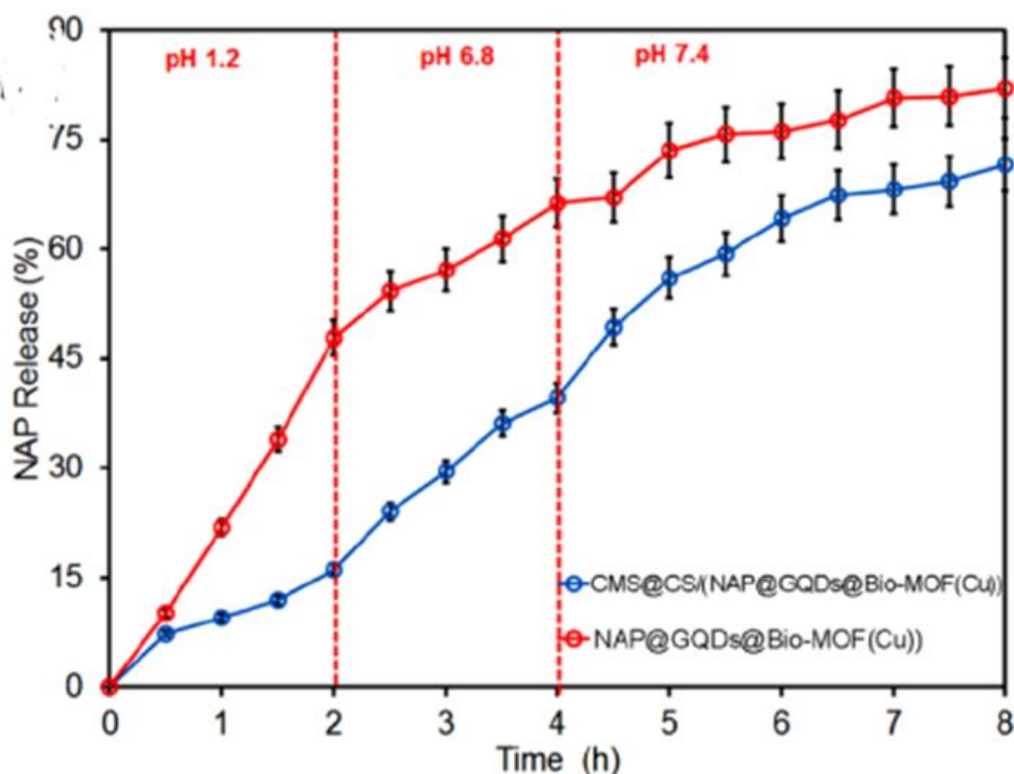
Figure 2.7: Comparison of the in vitro NAP release pattern from NAP@GQDs@Bio-MOF(Cu) and CMS@CS/ (NAP@GQDs@Bio-MOF(Cu)) at simulated GIT.

MOF by incorporating GQDs into the structure to 53.1%. In their research, drug release was studied at pH of 1.2, 6.8, and 7.4 (simulated GIT conditions), the GQD@Bio-

MOF showed fast release of the drug **(fig.2.7),** in order to overcome this limitation the GQD@Bio-MOF was coated with carboxymethyl and chitosan resulting in a slow and pH dependent drug release, making it one of the feasible oral drug delivery system for colon-specific drug delivery [56].

Zhang M at el, in their research combined the properties of silver MOF with chitosan nano particle by successfully incorporating chitosan nanoparticle into silver MOF synergistically increasing the anti-microbial activity of the system for enhanced wound healing applications. In order to improve the biocompatibility and reduce the cytoxicity, the MOF composite was covered with upper and lower layer of polyvinyl/sodium alignate/chitosan, avoiding direct contact of the silver MOF composite with the skin. Good example of increasing MOF efficiency by making its composite [57].
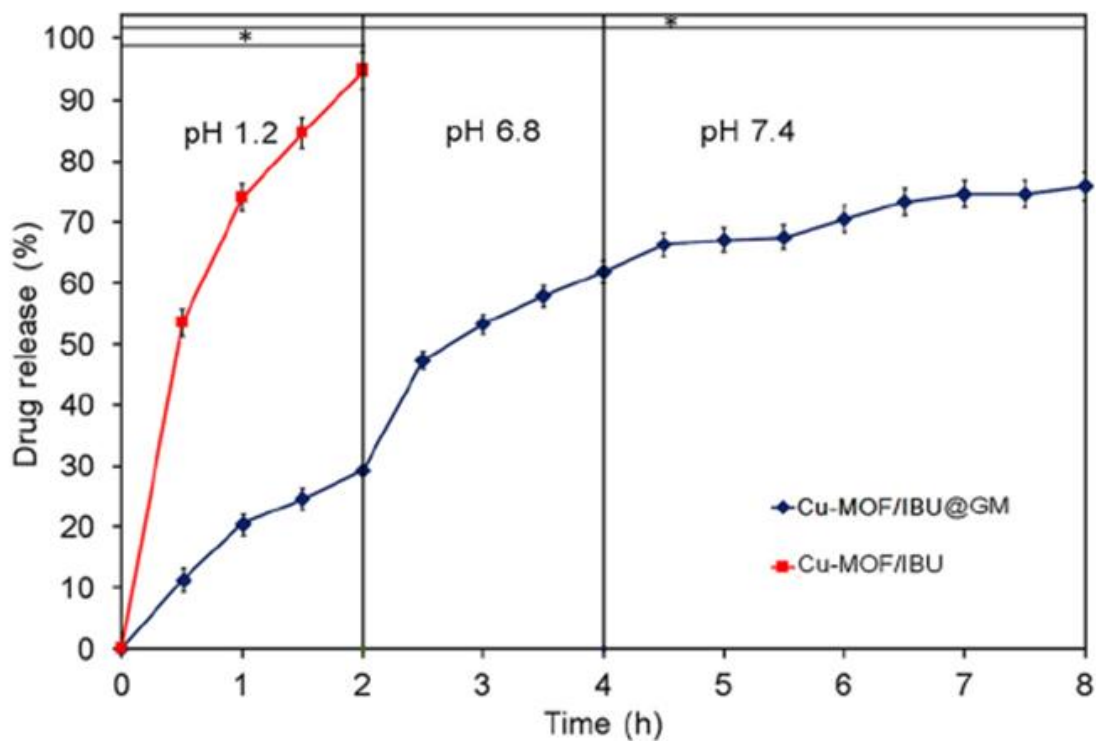
Figure 2.8: Drug release behavior of Cu-MOF/IBU and Cu-MOF/IBU@GM in conditions that simulates the gastrointestinal tract passage [73].

Hassanpouraghdam Y at el, In their research for the first time they synthesized complex polymer composite system for enhanced drug delivery. The system consisted of

bio cadmium MOF in which graphene quantum dots were incorporated and coated with biopolymer. The team was successful in increasing the overall encapsulation efficiency to 42.04% and controlling the drug release upto 62.03% in 92 hours incubation period. Hence, improving the overall capacity and release rate through combining the characteristics of bio-MOF, quantum's dots, and biopolymers [58].

Javanbakht at el successfully synthesized copper MOF nano hybrid systems coated with gelatin for oral delivery of ibuprofen. In this research they mainly focused on controlling the drug release rate by coating ibuprofen loaded copper MOF composite with gelatin that will work as a capping agent, for oral drug delivery. They were successful in achieving the results and the release percentage got decreased to 75% in 8 hours, through GIS fluid **(fig.2.8)** [59]**.**

Lin C at el, in the research developed a novel composition of Iron metal organic framework (MIL-100) with carbon quantum dots coated with O-carboxymethyl chitosan. They main focus of the research was to synthesize such oral drug delivery system that can be used for diagnostic as well as therapeutic simultaneously. They were successful in developing a biocompatible theranostic system by using magnetic and fluorescence properties of MIL-100 and carbon quantum dots respectively. 50% was the drug encapsulation efficiency they achieved with the help of this novel composition by synergistically combining the physiological characteristics of MIL-100, carbon quantum dots, and OCMC bio polymer. Due to the coating of OCMC the drug releasing capability of the system was also pH dependent and controlled [60].

2.4   Ibuprofen for Wound Healing Applications

IBP is a well-known NSAID that has anti-inflammatory, antipyretic, and pain-relieving qualities. It is also safe, effective, and well-tolerated. IBP functions by inhibiting the two isoforms of cyclooxygenase, COX-1 and COX-2, which are the enzymes in charge of prostaglandin manufacturing. Through oral treatment, the anti-inflammatory properties of IBU have been specifically investigated in osteoarticular, venous leg ulcers, and muscle recovery [61].

Pavaloiu et al, reported in their research the creation of PVA/CS complex composite films that were covered in many layers of bacterial cellulose to maintain the release of IBU. After twenty-five hours, the composite films allowed for the maximal release of IBU. Solvent casting, a labor-intensive process involving the use of organic solvents and extra purification stages, was used to create polymer films [62].

2.5   Research Gap

Wound healing systems based on advanced nano materials have become the need of the hour in order to fill the gap between the wound effected cases and efficient healing systems. For this purpose, polymer complex composite system consisting of MOF-199 filled with graphene quantum dots and coated with chitosan have been selected. All the materials mentioned have vast applications in the field of biomedical engineering due to their unique characteristics mentioned earlier. Such combinations have never been used for drug delivery, or very little data is available, especially in case of wound healing applications. The effect of Ibuprofen loaded onto this material is also being investigated for the first time in this research.

2.6   Research Objective

This research majorly focuses on the synthesis of N-doped graphene quantum dots imbedded in MOF-199 for wound healing applications. The large number of pores, tunable morphology, and functionalized surface area of MOF-199, when combined with biocompatible, non-toxic, and large surface area graphene quantum dots will synergistically enhance the drug carrying capability of the system. The GQD@MOF-199 polymer composite can increase the drug encapsulation efficiency due to the availability of large number of pores increasing the overall surface area, and due to the presence of amine and hydroxyl functional groups, it will electrostatically attach to large number of ibuprofen molecules, resulting in a controlled release.

To further control drug release, enhance biocompatibility, and for better attachments to the wound, the GQD@MOF-199 system will be coated with biodegradable polymer layer, chitosan. Chitosan is naturally occurring nontoxic anti-inflammatory, and anti-

bacterial polymer, that act as a capping agent and plays an important role in the control release of the drug.

In this research, the embedding of graphene quantum dots onto MOF-199 will be studied, coated with chitosan polymer. This research will mainly focus on the drug carrying and unloading capability of the system.

2.6.1 Objectives

The following objectives of this thesis are:

- Synthesis and characterization of MOF-199 and GQD@MOF-199 via in-situ hydrothermal route.

- Synthesis and characterization of chitosan@GQD@MOF-199 via beaker chemistry.

- Evaluation of drug loading and drug release behavior of MOF-199, GQD@MOF-199 and chitosan@GQD@MOF-199.

CHAPTER 3: MATERIALS AND METHODS

3.1   Material Utilized

L-glutamic acid, Copper nitrate trihydrate (Cu (NO$_3$)$_2$), Benzene Tricarboxylic Acid (BTC), Di-Methyl Formamide (DMF), Chitosan (CS), Phosphate Buffer Solution (PBS), Ethanol, Acetic acid, Ibuprofen (IBP), and DI water. All chemicals used were analytical grade without further purification.

3.2   Fabrication of Drug Delivery System

3.2.1   Synthesis of MOF-199

MOF-199 was synthesized according to the previously reported method with slight [63] change in the parameters. 2.76 gram of copper nitrate trihydrate (Cu(NO$_3$)$_2$) was added to 20 ml of DI water and stirred for 15 minutes. 1.33 gram of benzene trichloride (BTC) was added to 40 ml of absolute ethanol and DMF solution (1:1), stirred for 15 minutes. Both the solutions were combined, transferred to Teflon vessel, and placed in an autoclave for hydrothermal reaction at 120 ºC for 24 hours. After the reaction was completed MOF-199 was separated through vacuum filtration and washed with ethanol followed by DI water. The obtained sample was dried overnight in vacuum furnace at 60 ºC. Dried sample was collected and stored.

3.2.2   Graphene Quantum Dots

Graphene quantum dots were synthesized according to the previously reported method [64]. Typically, GQDs were synthesized by one-step pyrolysis of L-glutamic acid, A naturally occurring biocompatible amino acid making it suitable for biomedical applications. Briefly, 5.0 g of L-glutamic acid was added into a glass bottle and heated to 210 °C with a heating mantle. After 30 minutes the solid L-glutamic acid changed to liquid, the boiling colorless liquid turned brown, which indicated the formation of GQDs. Then, 30 mL water was added into the solution followed by stirring for 30 min to obtain brown

GQDs solution. The obtained solution of the GQDs was centrifuged at an rpm of 13000 for 15 minutes, and the supernatant was collected and stored for further use.

The concentration of the above solution was obtained via UV visible spectroscopy, which was equal to approximately 1M or 1mg/ml.

3.2.3 Synthesis of GQD@MOF-199

Three different compositions of GQD@MOF-199 were synthesized in which the concentration of the GQDs was varied. For preparing the composites of GQD@MOF-199, previously reported method was use with slight modification [65]. 3 solutions were prepared of 2.76 gram of copper nitrate trihydrate ($Cu(NO_3)_2$ added to 20 ml of DI water, and stirred for 15 minutes. 6, 10, 25 ml of the GQDs (1mg/ml) solutions in DI water were added individually to copper solutions prepared above and stirred for 15 minutes. The prepared solutions were added separately to 20 ml absolute ethanol and 20 ml dimethyl formamide (DMF) consisting of 1.33 grams of benzene tricarboxylic acid (BTC), stirred for 15 minutes. After stirring all of the above solutions were transferred to Teflon vessel, placed in autoclave for hydrothermal synthesis at 120 °C for 24 hours. Similar protocol was repeated as mentioned previously for the separation, purification, and storage as it was for MOF-199.

3.2.4 Drug Loading

Anti-inflammatory ibuprofen drug was taken as a model drug to estimate the load and release performance of GQDs@MOF-199 and MOF-199. Initially, the 10 mg of ibuprofen was added to ethanol (10 mL) and then stirred for 2 h to dissolve. Afterward, about 100 mg of GQD@MOF-199 of all the three compositions prepared, were added to the drug solution individually. The dispersion was stirred for 48 hours at room temperature. The ibuprofen loaded GQD@MOF-199 composites were separated from the free drug solution using a centrifuge at an rpm of 4500 for 15 minutes and rinsed with ethanol to remove the un-loaded drug. The supernatant was analyzed by UV–vis spectrophotometer at λmax of ibuprofen which was 264 nm. Then, the un-loaded ibuprofen content in the loading medium was calculated by an established ibuprofen calibration curve. In the end,

the Ibuprofen loading percentage was calculated by the below-described **equation number 3.1**. The same procedure was repeated for loading ibuprofen onto MOF-199 for comparison, and to the all of the composition of GQD@MOF-199 that were synthesized in the previous topic. [56], [66]**.**

$$Drug\ encapsulation\ effeciancy\ (w\%) = \frac{Mass\ of\ Ibuprofen\ in\ carrier}{Mass\ of\ Ibuprofen\ fed\ intially} x100 \quad (3.1)$$

3.2.5   Chitosan coating of IBU@GQD@MOF-199

Method for coating chitosan was used as previously reported with slight modification. 100 mg of chitosan was added to 25 ml of acetic acid (2%v/v), stirred for 24 hours at room temperature to uniformly distribute chitosan in the solution. After that 100 mg of IBU@(10mg)GQD@MOF-199 was added to 25 ml ethanol and stirred for 15 minutes. Both the solutions were mixed and stirred for 4 hours. The resulting chitosan coated GQD@MOF-199 were collected through centrifugation at 5000 rpm for 10 minutes and washed with acetic acid, DI water, and ethanol. Same was repeated for MOF-199 coating with chitosan process, but instead of using (10mg)GQD@MOF-199 composite, MOF-199 was used [67].

3.3   Release study of Ibuprofen

For the investigation of topical release profile of Ibuprofen from chitosan@IBU@(10mg)   GQD@MOF-199**,**   chitosan@IBU@MOF-199, IBU@GQD@MOF-199, and IBU@MOF-199, 4 glass beakers were taken containing 30 ml Phosphate buffer solution (PBS)(pH=7.4) at 37°C to mimic body fluid [68]. 100 mg of each material mentioned above were suspended in the beakers containing phosphate buffer solution and were stirred at 37°C bodily temperature in an incubator at an rpm of 80, 3 ml of the medium in which drug released occurred, was collected from each beaker after specific time interval of 3, 6, 24,48, and 72 hours, replaced with same volume of fresh buffer solution, to keep the volume of the solution constant [60]. The collected samples were examined by UV-visible analysis at 264 nm wavelength, a standard absorption

wavelength for ibuprofen [66]. Concentration of the UV analyzed solution were found with the help of standard IBU concentration curve.

CHAPTER 4: CHARACTERIZATION TECHNIQUES

4.1   XRD

A nondestructive method that can be used to identify residual stresses, elastic characteristics, and the identity of unknown materials in the lattice spacing of crystalline solids. Lattice spacing is calculated when x-rays with a known wavelength and angle enter a material, travel through atomic planes, and then refracted through to a diffractometer to measure intensity. In order to properly identify the planes present, X-rays are directed toward the sample at various angles to activate the planes at those distinct angles. It is common practice to identify the atomic spacing and Miller indices (hkl) of a powder sample by subjecting it to X-ray radiation. The measured intensities correlate to particular elements or phases. The sample exhibits several intensity peaks, indicating the presence of multiple constituents or phases.

A heated filament's electrons hit a copper target material, displacing the electrons in its inner shell and causing X-rays to be released. The resulting X-rays are collimated and focused onto the sample, where they deflect back to satisfy Brag's law (**fig.4.1**). A diffractometer then records the X-ray signals, turning them into counts (peaks) that are displayed on a computer screen.

The orientation of the various crystalline phases that are present can be determined using X-ray diffraction. It is also utilized for measuring the thickness of thin films and multilayer materials, as well as for determining structural factors such as strain, atomic arrangement, lattice parameters, and phase composition.

An XRD machine with an angle of 2θ is used to test a tiny sample of finely grind nano powder, which is then scanned from 0 to 75 degrees in order to evaluate the nanoparticles for structure and phase identification.
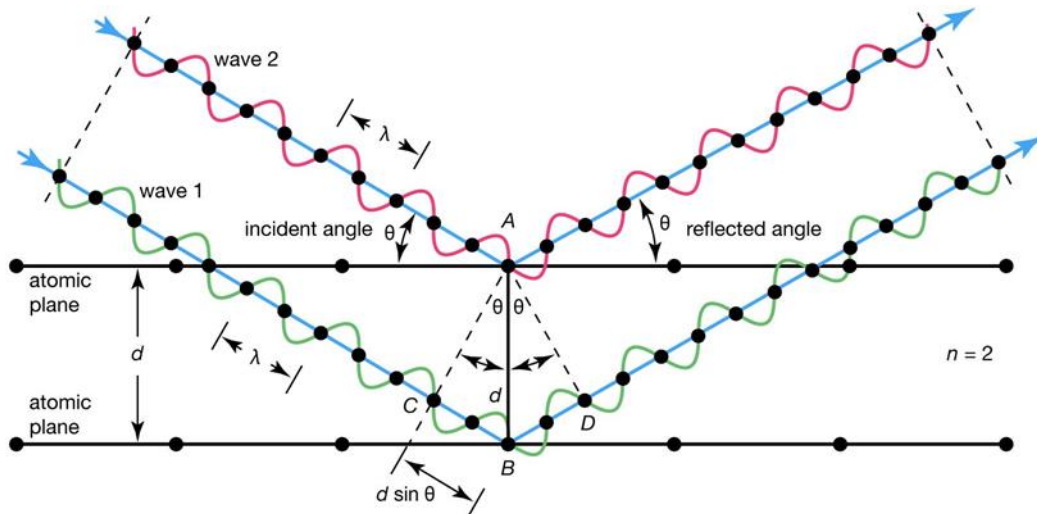
Figure 4.1: X-ray diffraction (XRD) working mechanism.

4.2   Scanning Electron Microscope (SEM)

This method uses high energy electron beams to generate range of signals. The material's crystalline structure, chemical makeup, orientation, and surface morphology are among the details analyzed by electron sample contact. Typically, a two-dimensional picture is produced that displays the sample surfaces' characteristics. A scanning electron microscope with a resolution of 50–100 nm and a magnification range of 20X–30000X can image an area as small as 5 microns. Energy dispersive X-ray (EDX) can be used for selective analysis, which is a method of determining chemical composition by scanning electron microscopy.

The interaction of accelerated electrons with the sample produces a range of signals. These signals include visible light, heat, photons (used for elemental analysis), backscattered electrons (used to indicate contrast in the composition), secondary electrons (used to determine morphology and topography), and photons. The SEM technique is regarded as "non-destructive" since it does not result in volume loss when producing distinct signals, allowing for repeated testing of the same sample.

27
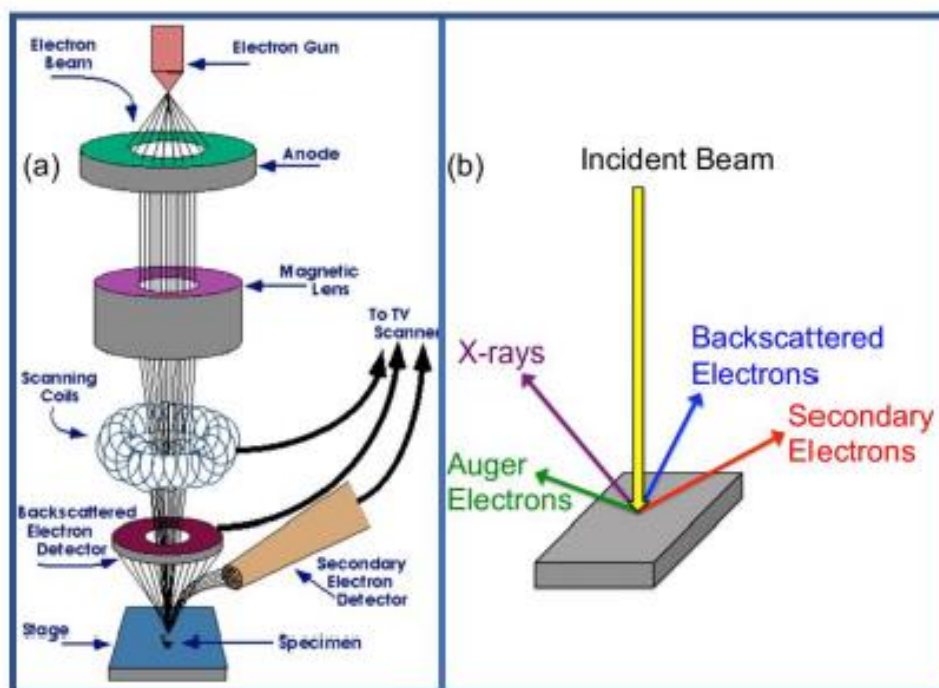
Figure 4.2: Experimental setup for scanning electron microscopy (a) Different rays reflected from the sample (b).

For the characterization of nano particles, the powder samples were taken and dried overnight in vacuum at 60 degrees centigrade. After drying the samples were finely grind in order to get accurate results. Then the samples were placed on a stub to gold plate it in order to make it conductive, placed in a vacuum chamber where the sample was plated with gold through sputtering. Images were taken at different magnification and resolution using a 20 kV voltage.

4.3   Zeta analysis

Electrokinetic potential in colloidal dispersions **(fig.4.3)** is scientifically known as zeta potential. It is commonly represented as ζ-potential in the colloidal chemistry literature, using the Greek letter zeta (ζ). The most widely used units are millivolts (mV) or volts (V). The electric potential in the interfacial double layer (DL) at the site of the sliding plane in relation to a point in the bulk fluid away from the interface is known as the

zeta potential from a theoretical perspective. Zeta potential, then, is the potential difference between the stationary fluid layer associated to the dispersed particle and the dispersion medium.

Zeta potential can now be measured with several novel instrumentation techniques. Powder, fibers, and solid materials can all be measured with the Zeta Potential Analyzer. The electrolyte solution flows through the sample in an oscillating pattern thanks to the instrument's motor. The equipment has multiple sensors that track additional variables, allowing the software that is attached to calculate the zeta potential. For this reason, the instrument measures temperature, pH, conductivity, pressure, and streaming potential.
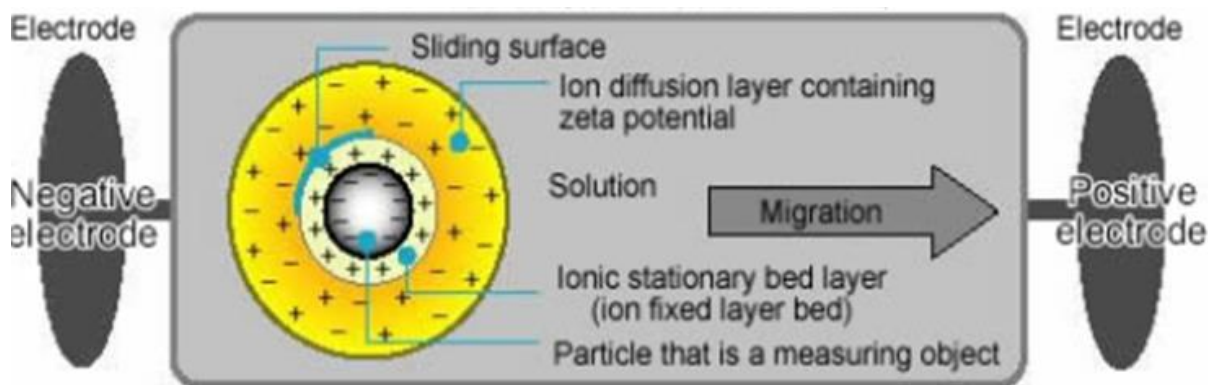
Figure 4.3: Inside of the cell (measurement container).

4.4   Spectrometry

4.4.1   Fourier Transform Infrared Spectroscopy (FTIR)

The idea behind FTIR **(fig.4.4)** is that materials absorb infrared radiation. The various wavelengths of infrared light that a material can absorb and utilize to calculate its molecular makeup and structure.

Using infrared rays from a spectrometer, the FTIR technique is used to identify the various functional groups that are present on the surface of the sample. This is done in the $4000cm^{-1}$ to $400cm^{-1}$ range.

Typically, samples are made by combining nanoparticles with potassium bromide (KBr) and then crushing the mixture into a pellet using a uniaxial press. This pellet is then utilized for characterization.
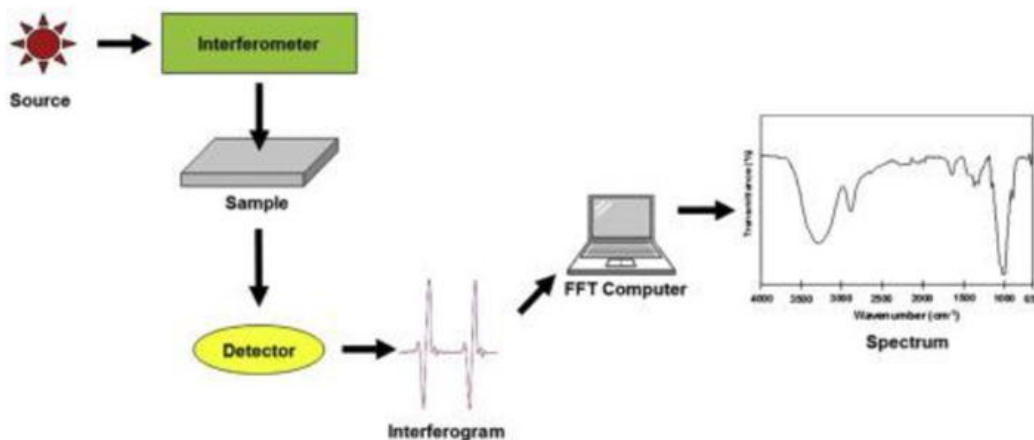
Figure 4.4: FTIR setup.

4.4.2   UV-Visible Spectroscopy

This method operates on the basis of comparing the sample's absorption of visible or ultraviolet light to that of a reference or blank sample, which yields information about the sample's composition (because different materials absorb light at different wavelengths) and concentration.

UV light is typically employed to characterize samples since it emits more energy (frequency) due to its shorter wavelength than visible light. A sample's greatest absorbance value at a particular wavelength can be used to determine the material's composition.

High intensity light sources, such as Xenon lamps **(fig.4.5)**, are used to produce light that is filtered using a monochromator to a desired wavelength and to increase the signal to noise ratio. The filtered light is then passed through a reference sample and from the sample that will be examined. Samples are held in quarter cuvettes.

Initially, the same medium used to fill the sample is utilized to fill the cuvettes holding the main sample and the reference. Following a single run, a cuvette holding a blank is swapped out for a solution containing the sample and the same solvent that was previously used for characterization. A detector picks up the signals, which are then shown on a monitor as a graph with absorbance (Y-axis) and wavelength (X-axis).
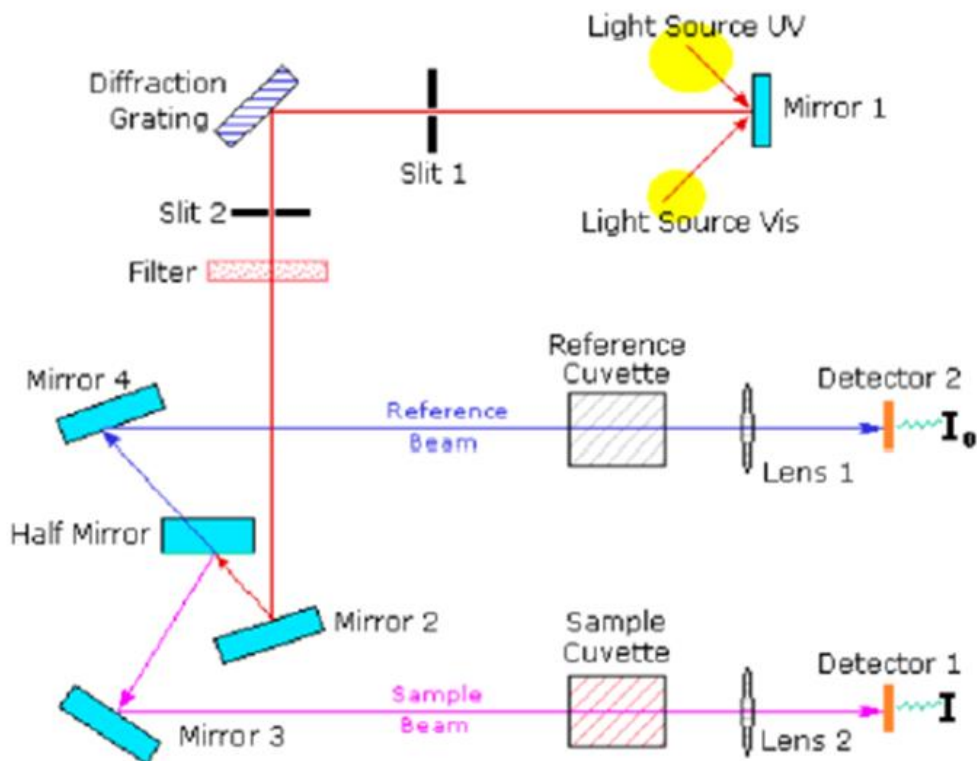
Figure 4.5: Path the UV takes.

The light intensity (I_o) prior to the sample passing through divided by the intensity after the sample passing through (I) is the identified absorbance value. The transmission values are obtained from the inverse relationship between these two quantities.

When data for path length, absorbance, and molar absorptivity are known, Beer-Lambert's law as shown in equation 4.1 can be used to calculate the sample's concentration in mol L^{-1}.

$$A = \varepsilon\, L\, c = \log_{10}\left(\frac{I_o}{I}\right) = \log_{10}\left(\frac{1}{T}\right) = -\log_{10}(T) \qquad \text{(4.1)}$$

All of the samples were diluted in deionized water with a solute to solvent ratio of 1 mg per milliliter in order to characterize the nanoparticles. The material was poured into quartz cuvettes, which were utilized to characterize the sample in the 200–500 nm range.

4.4.3 *Photoluminescence (PL) Spectroscopy*

The phenomenon known as photoluminescence (PL) occurs when a material absorbs photons, or electromagnetic radiation and subsequently emits photons again. The instrumentation used for PL **(fig.4.6)** is same as compare to the of UV spectrometry except that instead of analyzing absorbance it detects the emission spectra of a particular material at a specific wavelength.

According to quantum mechanics, this is equivalent to being excited to a higher energy state, returning to a lower energy state, and being accompanied by the discharge of a photon.

An electron can be raised from the valence band up to the conduction band across the forbidden energy gap by absorption of a photon of light with energy greater than the band gap energy. The electron typically has surplus energy throughout this photoexcitation process, which it loses before coming to rest at the lowest energy in the conduction band. The electron energy eventually returns to the valence band at this point.

this occurs, the energy that the substance loses is transformed back into a luminous photon that is released. Hence, the band gap energy can be directly determined from the energy of the released photon, for example. Photoluminescence is the process of excitation of photons followed by their emission.
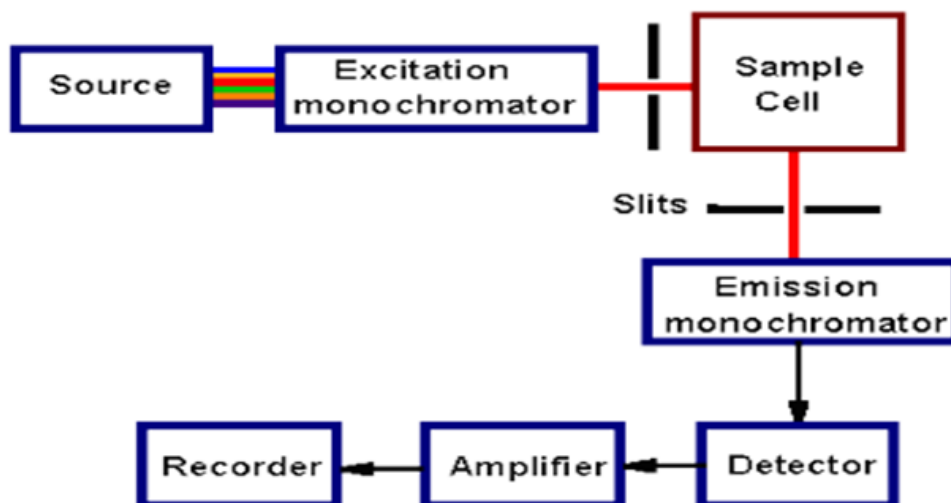
Figure 4.6: Instrumentation of PL spectrometry.

GQDs as prepared 1 mg/ml solution was characterized through PL spectrometry. The solution was excited at a wavelength of 365 nm and the value of emission was recorded from 400 nm to 600 nm.

CHAPTER 5: RESULTS AND DISCUSSION

5.1   Fluorescence properties of GQDs

The UV absorbance spectra as shown in the below **fig.5.1a** Clearly indicates two distinct peaks ranging from 231nm-248nm and a third peak at 290 nm, which clearly matches with absorbance spectra of the GQDs published. The two absorbance peaks ranging from 231 to 248 nm can be assigned to the transition of electrons between π-π^* and n-π^* between C=C and oxygen/nitrogen groups, the presence of sp^3 clusters resulted in the peak at 290nm [69], [70]. The maximum absorption of UV light was obtained at the wavelength of 232 nm equal to 5.31. The molecular absorption coefficient for GQDs is 5.5ml mg^{-1}cm^{-1} [64]. The concentration of the final GQDs solution was obtained with the help of **equation 2**. The final concentration of the GQDs solution obtained was **1 mg/ml**.

The graphene quantum dots showed a strong fluorescence peak as shown in **fig.5.1b** at around blue region (440nm-500nm), when excited by violet radiation (365 nm) Which confirms the successful formation of graphene quantum dots as the data matches the results already published in previous research papers [71]**.** Confirming successful formation of GQDs.
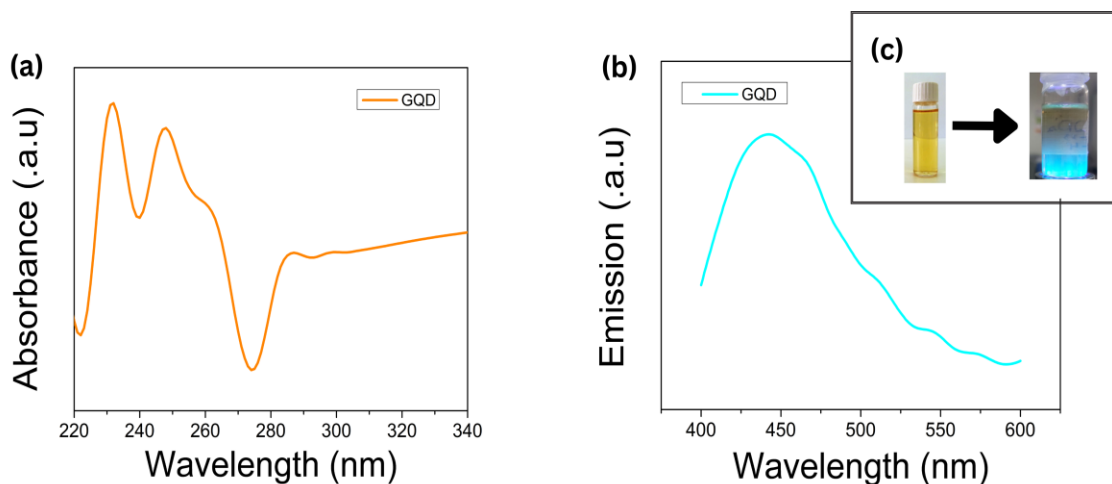
Figure5.1: UV absorbance spectra for GQDs (a), Emission spectra of GQDs at excitation wavelength of 365 nm (b)(c).

5.2 Fourier Transform Infrared Spectroscopy (FTIR)
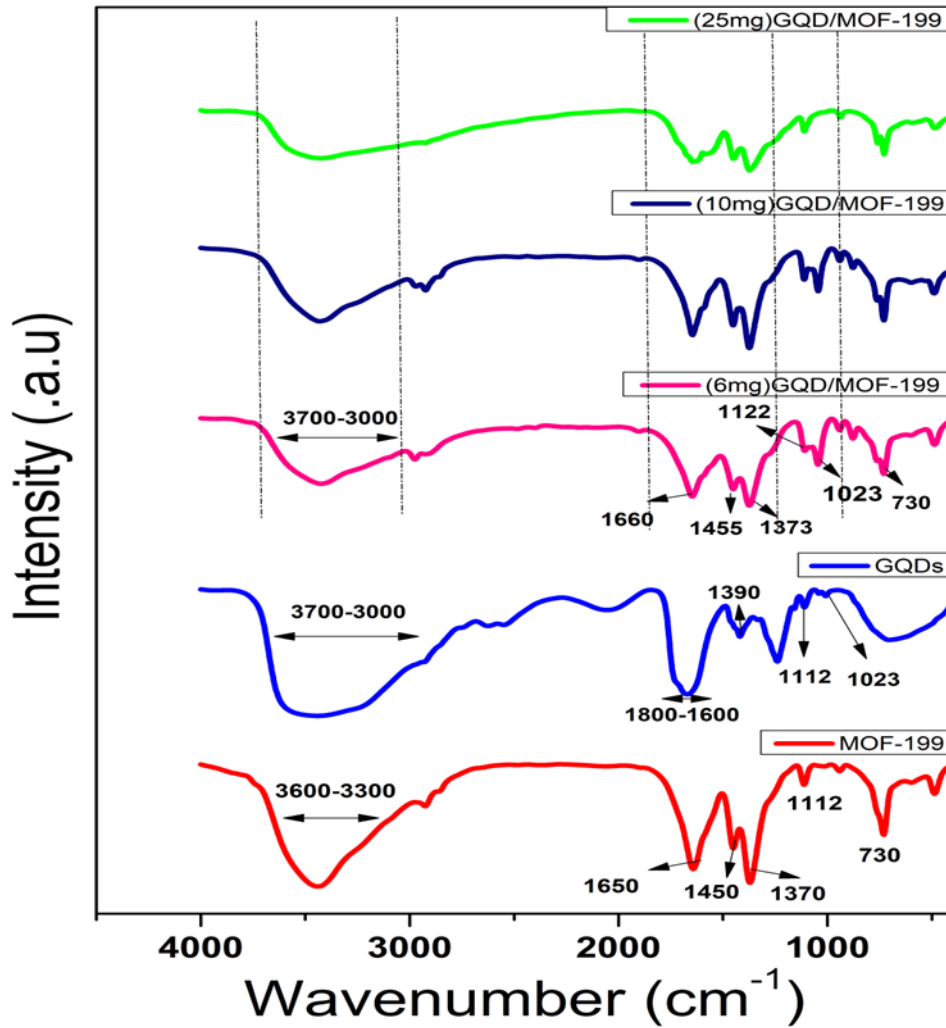
Figure5.2: FTIR spectra for MOF-199, GQDs, (6mg)GQD@MOF-199, (10mg)GQD@MOF-199, (25mg)GQD@MOF-199.

5.2.1 MOF-199

The FTIR spectrum MOF-199 **fig.5.2** showed a characteristic peak at ≈ 730 cm^{-1} corresponding to the C-H bending vibrations. Additionally, the characteristics band at $\approx$ 1112 cm^{-1} represent C-OH stretching vibration [72]. While the low intensity peak at $\approx$758 cm^{-1} was assigned to C-C ring out of plane bending modes. The stretching bands that

confirm the formation of Cu-MOF structure are ≈1650, ≈1450, and ≈1370 cm^{-1} which correspond to bridging bidentate formation of Cu-BTC in the composite [73].

5.2.2   Graphene Quantum Dots

The FTIR spectrum of graphene quantum dots in **fig.5.2** displayed a broad peak at ≈3700-3000 cm^{-1} due to the stretching formation of amides between amines and carboxyl groups merge with the stretching vibration of N-H groups, =CH of aromatic compounds, and with the stretching vibration of O-H group [68], [71].

The presence of peak at 1800-1600 cm^{-1} indicated asymmetric stretching vibration of C=C which confirms the formation of graphene quantum dots [56], [65], [71]. Stretching vibration of C-OH originated peak at ≈1122 cm^{-1}, and C=O stretching vibration peak was observed at ≈1393 cm^{-1}, Indicating presence of carboxyl groups. The C-N stretching vibration peak was observed at 1023 cm^{-1} showing the presence of amide linkage in the synthesized graphene quantum dots.

5.2.3   GQD@MOF-199

Fig.5.2 shows the FTIR spectra of GQD@MOF-199 for three different compositions consisting of 6, 10, and 25 mg of GQD added into MOF-199 during in-situ synthesis. The broad peak from the range 3700-3000 cm^{-1} indicates the presence of -NH$_2$ and O-H stretch. The presence of peak at 2950 cm^{-1} is due to the C-H bonding of the aromatic carbon.

The peaks at 1660, 1455, and 1373 cm^{-1} appeared because of the formation of copper bidentate formation with oxygen of BTC, merge with the bending vibration of N-H. The peak at 1122 cm^{-1} and 1023 cm^{-1} appeared because of the stretching vibration of C-OH and C-NH. All of the major peaks present in the FTIR spectra of MOF-199 (figure 23) and GQD (figure 24) were present in the spectra of the GQD@MOF-199 for all the compositions synthesized with a slight shift towards the higher wave number pointing towards the fact that Cu-MOF have anchored to the GQDs by forming coordinate covalent bond [56], [71], [72].

Figure5.3: FTIR spectra for IBU, IBU@MOF-199, IBU@(6mg)GQD@MOF-199, IBU@(10mg)GQD@MOF-199, IBU@(25mg)GQD@MOF-199.

The FTIR peaks for ibuprofen in **fig.5.3** clearly indicates the presence of O-H, symmetric and asymmetric C-H vibration stretch, ranging from 3400-2500 cm^{-1}. Similarly, the presence of peak at 1717 cm^{-1} shows the presence of -COOH bond. The peak at 1393 cm^{-1} corresponds to C=O bond confirming the presence of carboxylic group, the peak observed at 1428 cm^{-1} was for C-C stretching vibration in the aromatic rings [66], [68]. The FTIR spectrum of IBU@MOF-199 is a combination of both the individual spectrums. The increase in the O-H peak wavenumber from 2800 cm^{-1} to 3400 cm^{-1} with respect to the IBU FTIR curve and decrease in the characteristics peaks wavenumber of copper

coordination bonding with the oxygen of the carboxyl group from 1660 cm^{-1} to 1634 cm^{-1}, 1450 cm^{-1} to 1440 cm^{-1}, and 1370 cm^{-1} to 1360 cm^{-1} in ibuprofen loaded MOF-199 was observed in with respect to MOF-199 FTIR curve, reveals the formation of hydrogen bonds between the carboxylic and hydroxy group of ibuprofens and MOF-199. The increase in the intensity of the aromatic C-H bonding at 2924 cm^{-1} as compared to both previous graphs can be due to the presence of ibuprofen in MOF-199. Similar shift in the wavenumber of the copper coordination bond with oxygen of the hydroxyl group towards the lower values can be observed in all the composition of the ibuprofen loaded GQD@MOF-199, justifying the fact that ibuprofen was successfully loaded onto the MOF-199 and GQD@MOF-199.

5.2.5   *Chitosan Coated IBU@GQD@MOF-199 and IBU@MOF-199*
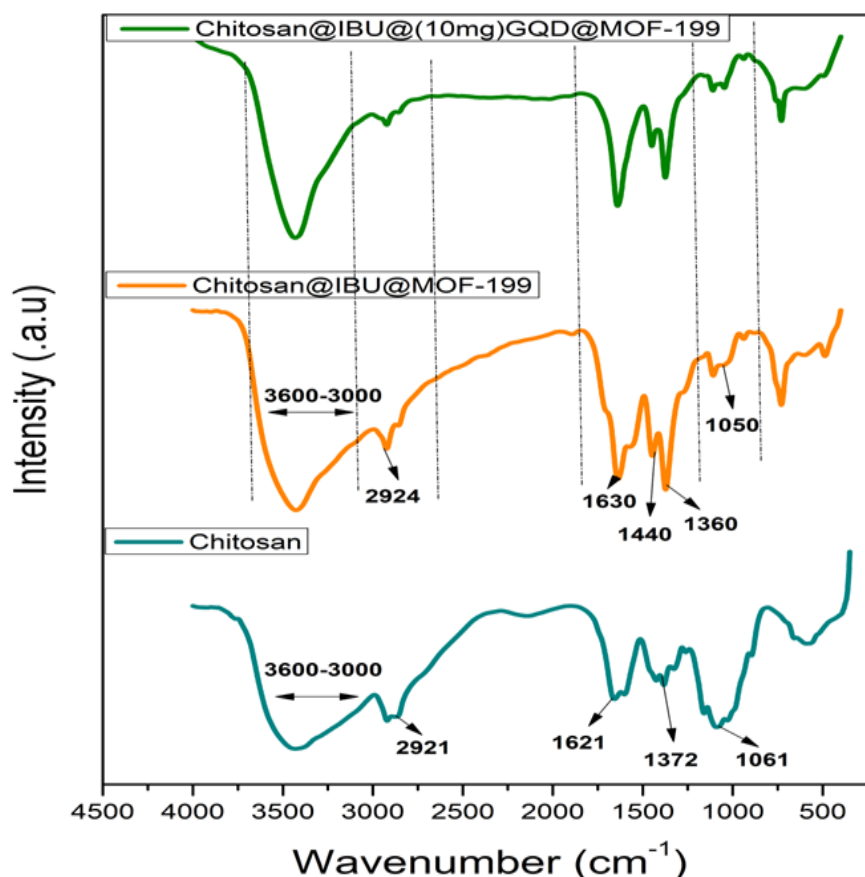
Figure5.4: FTIR spectra for chitosan, chitosan@IBU@MOF-199, chitosan@IBU@(10mg)GQD@MOF-199.

38

Characteristic peaks of chitosan in **fig.5.4** were observed at $\approx$2921 cm^{-1} indicating presence of vibrational C-H stretch, peak located at $\approx$1621 cm^{-1} represented N-H bending stretch. Peak located at $\approx$3424 cm^{-1}, $\approx$1372 cm^{-1}, are attributed to O-H, C=O stretching vibrations [57], [67]**.**

The peak 1061 cm^{-1} appeared because of the C-N Stretch. The composite of Chitosan@IBU@MOF-199 exhibits all the characteristics peaks for both Chitosan and IBU@MOF-199.

The stretching peak at $\approx$1630 cm^{-1}, 1440 cm^{-1}, 1360 cm^{-1} in the composite clearly demonstrates the presence copper bidentate formation with the carboxyl group of the linker, indicating the presence of IBU@MOF-199, the peak at 1050 cm^{-1} is due to the C-N stretch, confirming the formation of Chitosan@IBU@MOF-199.

The synthesized chitosan@IBU@(10mg) GQD@MOF-199 clearly exhibits all the characteristics peaks of the individual components present in the complex polymolecular structure.

Moreover, the band related to C-H and C-N stretch got more intense, it can be due to the CH$_2$ and C-N peaks of chitosan and GQDs, the FTIR peak at $\approx$3438 cm^{-1} for the O-H groups of GQD@MOF-199 shifted towards the lower frequency of $\approx$3390 cm^{-1} Indicating the formation of hydrogen bonds.

Considering the above data, it clearly indicates the successful formation of chitosan@IBU@MOF-199 and chitosan@IBU@(10mg) GQD@MOF-199.

5.3   XRD

5.3.1   MOF-199 and GQDs

As shown in **fig.5.5**, the diffraction peaks of the prepared MOF-199 were located at $2\theta = 5.79°$ (111), 6.69° (200), 9.5° (220), 11.66° (222), 13.46° (400), 14.3° (331), 16.48° (422), 17.48° (511), 19.06° (440) all the peaks matched well with the peaks of MOF-199 in the literature and in the International Centre for Diffraction Database (PDF no. 00-065-

1028), having a face centered crystal structure [73], [74], [75],[76]. The XRD peak for the Graphene quantum dot figure 28(b) was located at 2 θ =22.5° corresponding to (002) plane (JCPDS Card No:75–0444) indicating the presence of graphitic carbon and similar to the result obtained previously in the literature [77][56], [78]. The presence of a single peak points out that only one phase is present in the structure. So according to the literature we can conclude from the XRD result, the successful formation of GQDs.
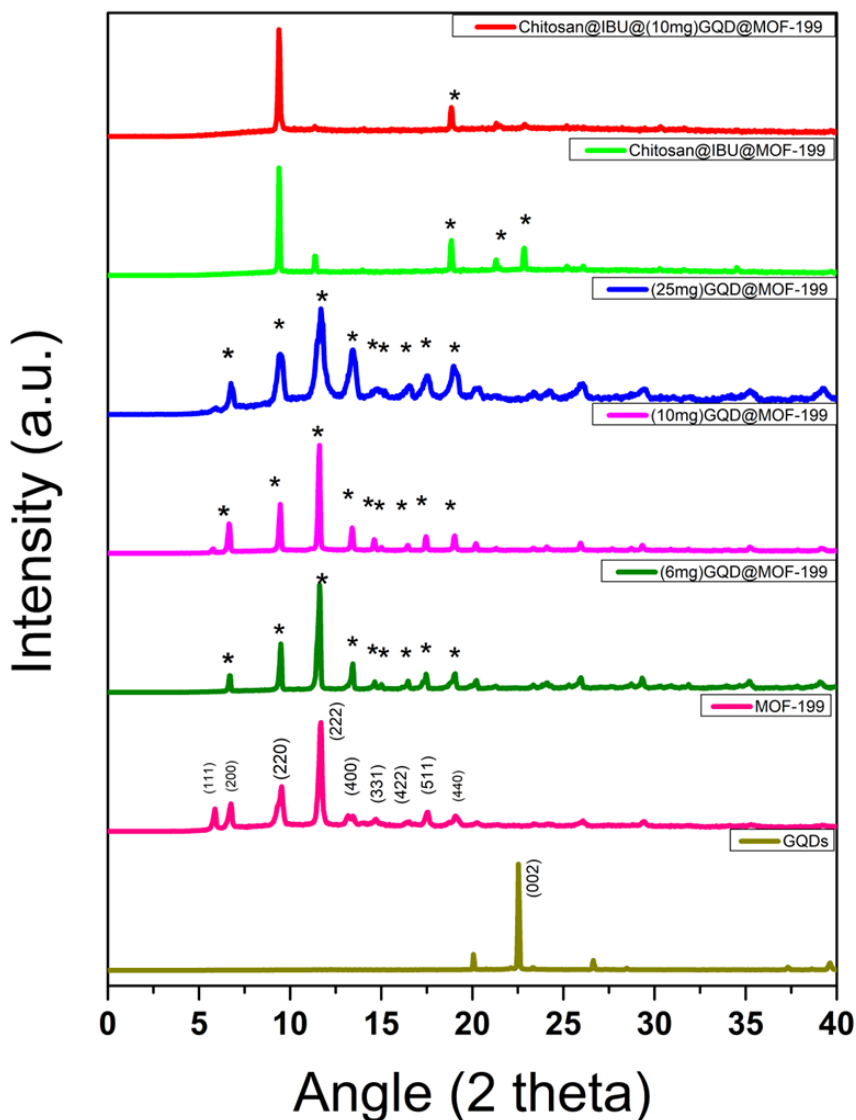
Figure5.5: XRD spectra for GQDs, MOF-199, (6mg)GQD@MOF-199,
(10mg)@GQD@MOF-199, (25mg)GQD@MOF-199.

5.3.2 GQD@MOF-199

The XRD pattern obtained in **fig.5.5** for all the composition of the GQD@MOF-199 shows similar XRD pattern obtained for MOF-199 which is $2\theta = 5.79°$ (111), 6.69° (200), 9.5° (220), 11.66° (222), 13.46° (400), 14.3° (331), 16.48° (422), 17.48° (511), 19.06° (440), and it proves that the structural integrity of MOF-199 was still intact after the in-situ formation of GQD@MOF-199. However, there are no obvious peaks for GQDs, it can be mainly due to the dispersion of small quantity of GQDs in the MOF-199. Due to the addition of GQDs into MOF-199 the peaks got more sharper indicating formation of large grain size which can be resulted from carboxyl and amine functional groups present in GQDs anchoring with copper and oxygen clusters of MOF-199[56], [78], [79].

5.3.3 Chitosan Coated IBU@MOF-199 and IBU@GQD@MOF-199

The XRD pattern of chitosan@IBU@MOF-199 and chitosan@IBU@GQD@MOF-199 in **fig.5.5** clearly shows the characteristic low intensity peaks of amorphous material, from $2\theta = 18°\text{-}25°$ which can be due to the crosslinking points in the structure, the disappearance of all the MOF-199 and GQDs peaks can be the result of chitosan covering all the surface of the MOF-199 and its composite, clearly indicating successful coating of chitosan onto the Cu-MOF, and Cu-MOF@GQD composite [56].

5.4 Scanning Electron Microscopy

5.4.1 MOF-199

The above **fig.5.6** shows the MOF-199 that was synthesized through hydrothermal method and was dried at 60°C in order to evaporate moisture so that clear SEM images can be obtained. After drying the powder sample was placed on a conductive stub, coated with gold through sputtering to complete the conductive path which is necessary for the SEM analysis. The clear crystal octahedral bi-pyramidal structure of the MOF-199 can be clearly seen in the images, size ranging from 10-15 μm, which indicates successful formation of the MOF-199 as mentioned in the previous literature[74], [78], [79]. The high porosity can

be observed on the surface of MOF-199 resulting in high surface area, making it a suitable candidate for the application of a drug carrier.
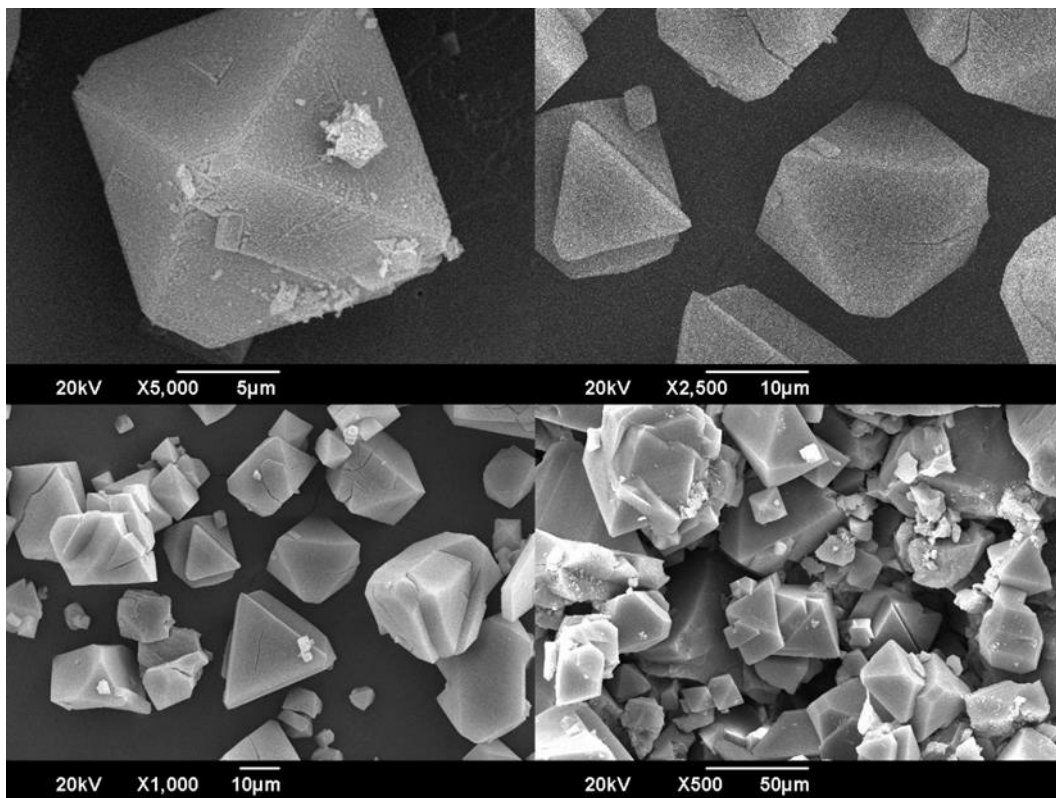
Figure5.6: SEM images of MOF-199 at different magnification.

5.4.2   GQD@MOF-199

5.4.2.1 (6mg)GQD@MOF-199

The (6mg)GQD@MOF-199 particle synthesized from in-situ hydrothermal technique can be observed in the above **fig5.7**. If we compare the images of the neat MOF-199 with the images of the (6mg)GQD@MOF-199 it clearly shows that MOF-199 have partially retained its crystal structure.

More investigation of the SEM images shows that incorporation of the GQDs into the MOF-199 have altered the external morphology of the MOF-199 as the composite is formed.

The texture of the morphology has gotten a little bit rough, and the particles are irregular in shape as compared to the pure MOF-199 [58].
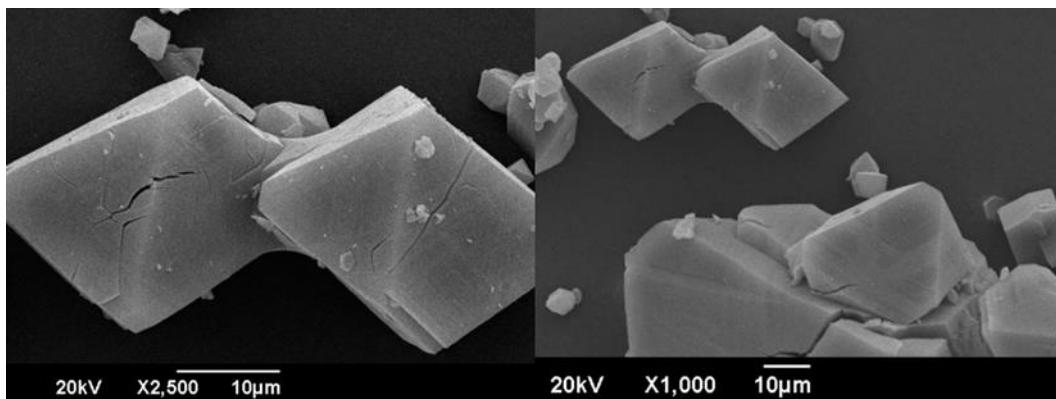
Figure5.7: SEM images at different magnification for (6mg)GQD@MOF-199.

5.4.2.2 (10mg)GQD@MOF-199
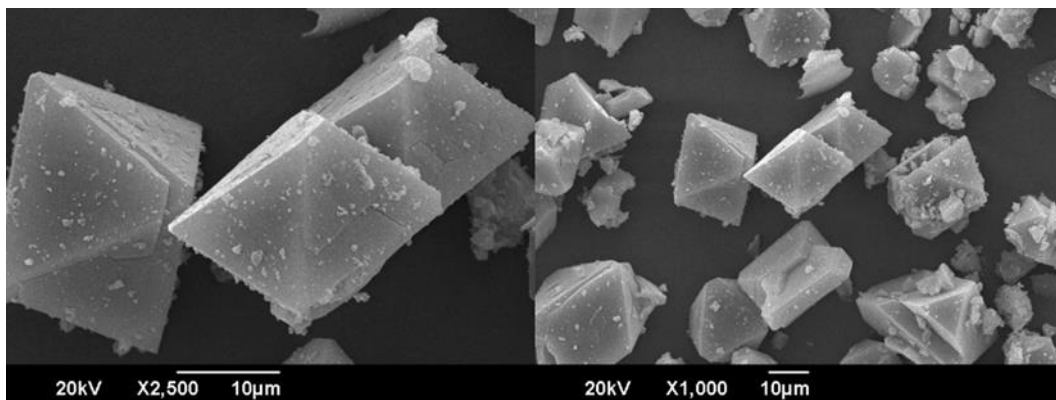
Figure5.8: SEM analysis of (10mg)GQD@MOF-199 at different magnification.

As we increase the amount of GQDs to 10 mg in the composite (10mg)@GQD@MOF-199 the crystallinity of the structure is partially intact as shown in **fig.5.8**.

But as the concentration increased the surface morphology changed as compared to the neat MOF-199. With an increase in the concentration of the GQDs, surface of the MOF-199 got rougher.

5.4.2.3 (25mg)GQD@MOF-199
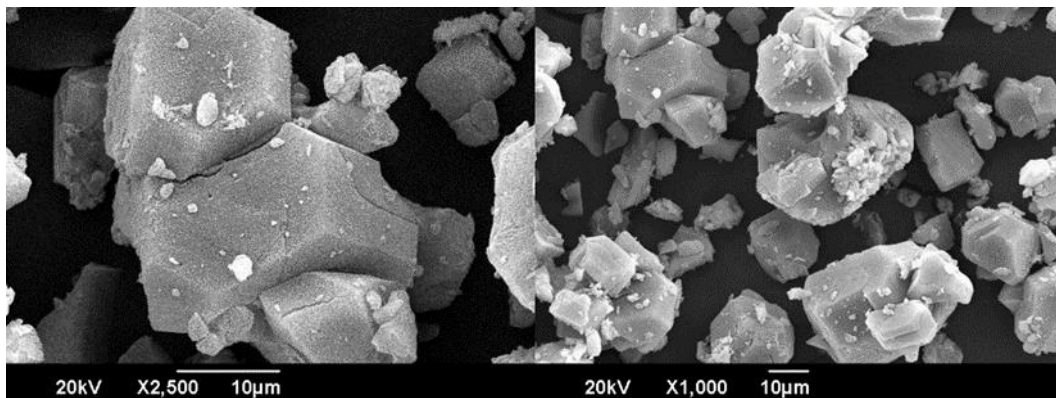
Figure5.9: SEM analysis of (10mg)GQD@MOF-199 at different magnification.

As the amount of the GQDs in the MOF-199 is increased to 25 mg the surface of the composite loses its majority of the crystallinity in **fig.5.9** and the roughness increases as compared to the previous two concentration and neat MOF-199, due to the increase in the GQDs in-situ incorporation into the MOF-199 structure.

5.4.3   Chitosan coated IBU@MOF-199 and IBU@GQD@MOF-199

5.4.3.1 Chitosan coated IBU@MOF-199
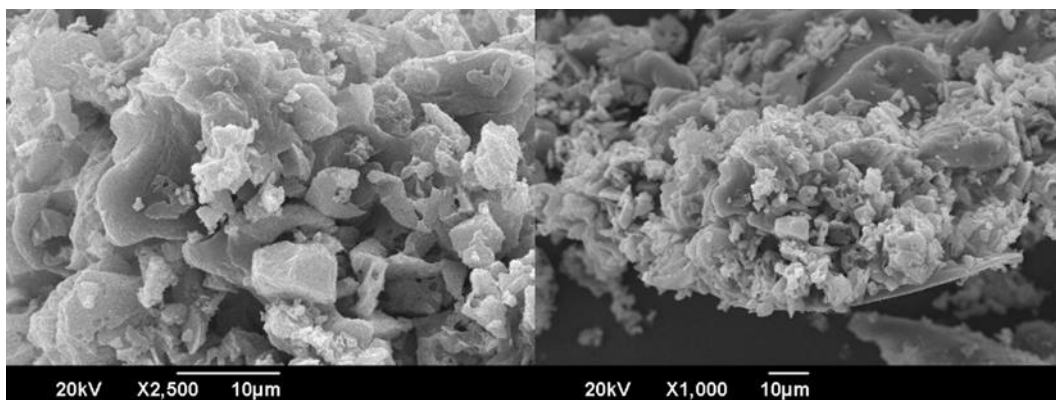
Figure5.10: SEM analysis of Chitosan@IBU@MOF-199.

In the above **fig.5.10** at different magnification chitosan coated IBU@MOF-199 shows binary structure of chitosan and IBU@MOF-199 wrapped around together forming agglomerated clusters of chitosan@MOF-199[56] Hence proving the successful coating of chitosan onto the IBU@MOF-199.

5.4.3.2 Chitosan Coated IBU@GQD@MOF-199
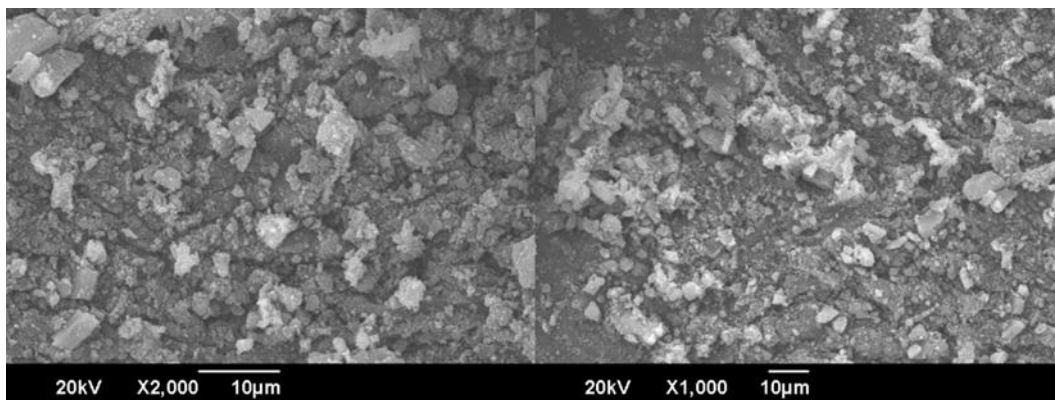
Figure5.11: SEM images at different magnification for chitosan coated
IBU@GQD@MOF-199.

The above **fig.5.11** shows the bead formation for the successful coating of chitosan on the ternary structure of IBU@GQD@MOF-199. Rough fibrous structure with agglomeration forming large clusters and totally covering the partially crystalline porous structure of the IBU@GQD@MOF-199, which was previously proved by the FTIR analysis.

5.5   Zeta Analysis

For the zeta analysis all the samples were prepared in DI water. The liquid samples were transferred to glass cuvette one by one for analysis. **Fig.5.12** shows the zeta potential in mV of the GQDs, MOF-199, (6mg) GQD@MOF-199, (10mg)GQD@MOF-199, (25mg)GQD@MOF-199, chitosan@IBU@MOF-199, and chitosan@IBU@GQD@MOF-199. The charge obtained on synthesized graphene quantum dots was -31mV due to the presence of amine, hydroxyl and carboxyl groups [80]**.** According to the literature,

graphene quantum dots show more stability if the zeta value is more than -30mV, zeta potential greater than -30mV is required for more stable colloidal graphene quantum dots solution [81].
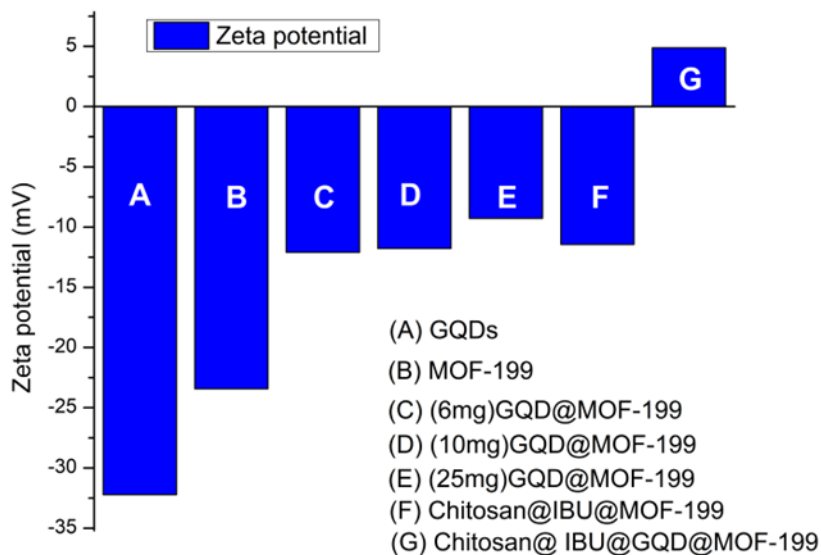
Figure5.12: Zeta Analysis of GQDs, MOF-199,(6mg)GQD@MOF-199, (10mg)GQD@MOG-199, (25mg)GQD@MOF-199, chitosan@IBU@MOF-199, chitosan@IBU@GQD@MOF-199.

The MOF-199 shows a negative charge of 22mV due to the presence of Carboxyl groups, but as compared to the N-doped GQDs the charge is less negative due to absence of amine groups [82]. The charge value of the polymer complex composites that were formed increased to a less negative value in case of (6mg)GQD@MOF-199, (10mg)GQD@MOF-199, (25mg)GQD@MOF-19. As the quantity of the GQDs increased in the composite the charge decreased and became less negative, this result indicate the protonation of the carboxyl groups by the amine groups present in GQDs, and as the concentration of the GQDs increase the number of amine group increased, resulting in more negative value. Chitosan@IBU@MOF-199 in spite the presence of positive chitosan group, because the positive effect of chitosan was cancelled out by ibuprofen loading which

46

also consist of negative hydroxyl groups. Positive value in case of chitosan@IBU@GQD@MOF-199, the reason behind an increase in overall charge value could be the protonation of the oxygen containing functional groups of MOF-199 in the presence of amine groups of GQDs and chitosan, justifying the in-situ presence of GQDs and chitosan coating onto MOF-199. The zeta results establish that the overall charge decrease was due to the successful formation of complex polymer composite [83].

5.6   Drug Loading

MOF-199 particles and GQD@MOF-199 particle consisting of 6, 10, and 25 milligrams of GQDs were loaded with ibuprofen. For preparing the samples 10 mg of ibuprofen was loaded onto 10 ml of ethanol making 10 mg/ml solution. In this solution all of the above mentioned particles were added separately at room temperature and stirred for 48 hours, then centrifuged. The supernatant was collected and was analyzed through UV-spectrometry for ibuprofen content in the solution with respect to the standard ibuprofen absorbance wavelength at 264 nm.

5.6.1   Beer Lambart Curve for Ibuprofen

Table 5.1: Absorbance value of ibuprofen at different concentrations

S.no	Concentration mg/ml	Absorbance
1	0.2	0.3881
2	0.4	0.73148
3	0.6	1.07489
4	0.8	1.4131
5	1.0	1.7617

Plotting the graph between absorbance and concentration allowed for the determination of the Ibuprofen standard beer lambert curve **(fig.5.13)**. using several dilutions.

Solutions containing 0.2 mg/ml, 0.4 mg/ml, 0.6 mg/ml, and 0.8 mg/ml and 1 mg/ml were produced in ethanol in order to determine the Ibuprofen standard curve. To determine the amount of medication at various dilutions, absorbance was measured at 264 nanometers **(table 5.1)**.
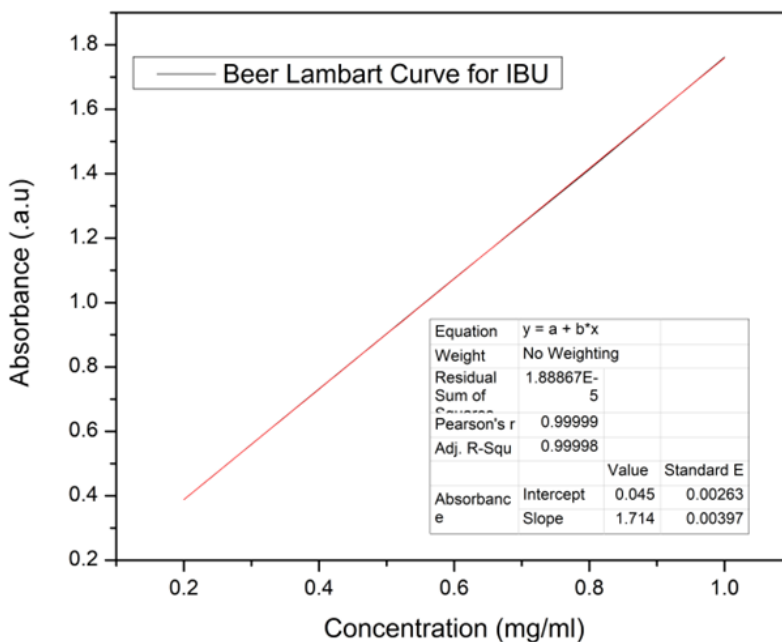
Figure5.13: Beer Lambart curve for IBU.

5.6.2   Ibuprofen Loading onto MOF-199 and GQD@MOF-199

$$\textbf{Drug encapsulation effeciancy }(\textbf{w}\%) = \frac{\textit{Mass of Ibuprofen in carrier}}{\textit{Mass of Ibuprofen fed intially}} \textbf{x100} \quad (5.1)$$

The remaining amount of the drug was calculated with the help of the absorbance value at 264 nm determined with the help of UV-Analysis. The calculated value of the absorbance was compared with beer lambert curve of ibuprofen to find the final concentration of the solution and by using above equation 5.1 the encapsulation efficiency was found. Encapsulation efficiency values calculated in the figure below.
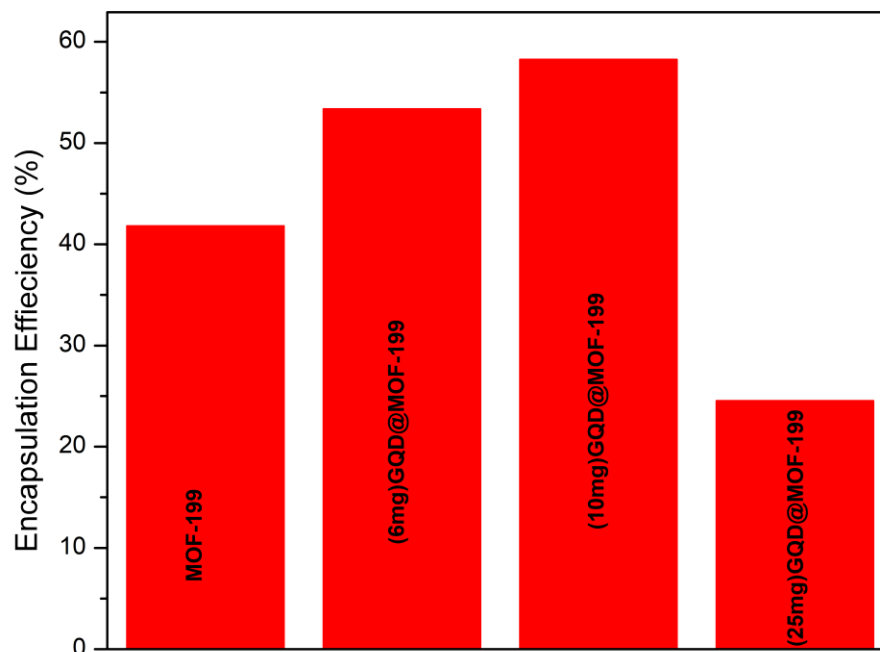
Figure5.14: Ibuprofen encapsulation efficiency bar chart for MOF-199 and (6mg)GQD@MOF-199, (10mg)GQD@MOF-199, (25mg)GQD@MOF-199 composites.

Table 5.2: Ibuprofen encapsulation efficiency table for MOF-199 and GQD@MOF-199 composites.

S.no	Material	Absorbance value	Relative drug weight(mg/ml)	Initial drug weight(mg/ml)	Encapsulation effeciency(%)
1	MOF-199	1.0437	0.581835124	1	41.81648758
2	(6mg)@GQD@MOF-199	0.8454	0.46634635	1	53.36536502
3	(10mg)@GQD@MOF-199	0.7613	0.417366996	1	58.26330043
4	(25mg)@GQD@MOF-199	1.3403	0.754573251	1	24.54267494

Drug loading efficiency is one of the important parameters in determining whether the newly introduced material is suitable for carrying a specific drug or not [56]. In this research the model drug selected was ibuprofen, an anti-inflammatory drug for wound healing application, that was loaded onto the MOF-199 and different compositions of

GQD@MOF-199, by dispersing both materials in the 1mg/ml ibuprofen solution. As shown in **(table 5.2)** the drug loading and encapsulation efficiency obtained were 41.82% for MOF-199, 53.37% for (6mg)GQD@MOF-199, 58.26% for (10mg)GQD@MOF-199, and 24.54% for (25mg)GQD@MOF-199.

There can be few possible explanations of Ibuprofen entrapment in MOF-199 and an increase in the encapsulation efficiency of GQD@MOF-199 at different compositions **(fig.5.14)**. The entrapment in the MOF-199 can be mainly due to the highly porous structure of MOF-199, while the increase encapsulation in (6mg)@GQD@MOF-199, (10mg)@GQD@MOF-199, and can be caused by the π-π interaction present in the benzene ring and the amine functionalized group present in GQD with the hydroxyl groups of Ibuprofen, synergistically working with the porous site of the MOF-199. Due to the increase in the concentration of GQDs in the MOF-199 the overall surface area and more functional sites are available for ibuprofen to electrostatically bond with. But as the concentration of the GQDs increases in (25mg)@GQD@MOF-199, it possibly blocks the inner pores of the MOF-199 during in-situ formation, disturbing the equilibrium, and resulting in the decrease encapsulation efficiency of the system. However, due to the presence of electrostatic interactions and hydrogen bonds between the polar groups present in Ibuprofen and (10mg)GQD@MOF-199 composites, the overall entrapment of the drug increases, making it a suitable composition to be used as a drug carrier for biomedical applications.

5.7 Drug Release Analysis

Table 5.3: Cumulative and percentage drug release data of loaded particles.

Time(Hrs)	MOF-199		GQD@MOF-199		Chitosan@MOF-199		Chitosan@GQD@MOF-199	
	CC (mg/ml)	% released	CC (mg/ml)	% released	CC (mg/ml)	% released	CC (mg/ml)	% released
3.0000	0.1352	97.0313	3.0181	51.8571	0.6524	11.2096	0.0166	11.9293
6.0000	0.1403	100.0000	3.1264	53.7184	1.0193	17.5139	0.0567	40.3106
24.0000			3.4147	58.6717	2.5883	44.4721	0.0562	40.7286
48.0000			3.9423	67.7379	3.7065	63.6851	0.0601	43.1111
72.0000			4.3337	74.4624	3.9651	68.1281	0.0710	50.9692
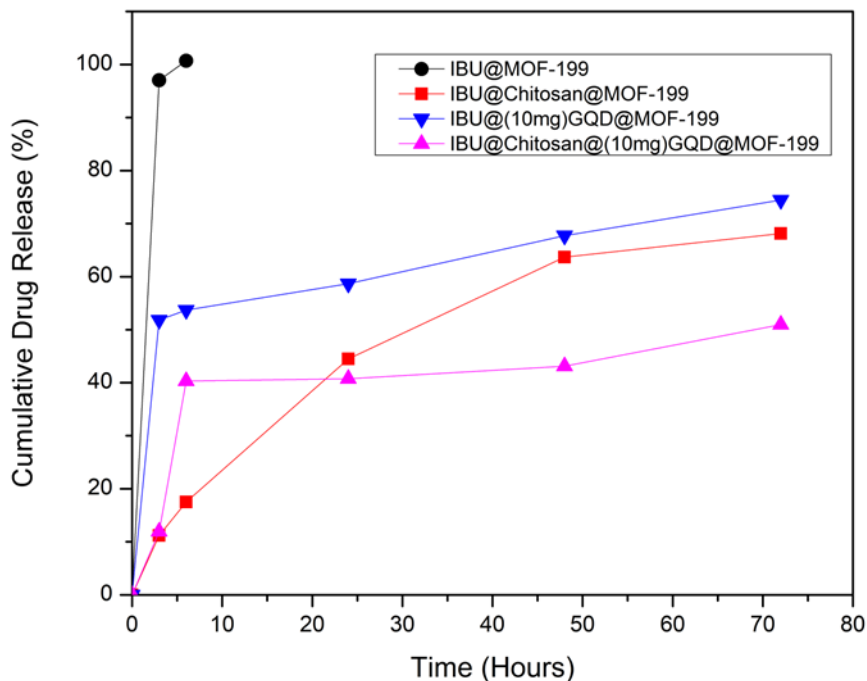
Figure5.15: Cumulative drug release percentage graph of IBU@MOF-199,
IBU@(10mg)GQD@MOF-199, chitosan@IBU@MOF-199,
chitosan@IBU@(10mg)GQD@MOF-199.

In the following, in-vitro drug release of ibuprofen was conducted in the body simulated fluid by using PBS buffer solution (pH=7.4) at 37^0C at an rpm of 80 in an incubation chamber, for IBU@MOF-199, IBU@(10mg)@GQD@MOF-199, chitosan@IBU@MOF-199,chitosan@IBU@(10mg)GQD@MOF-199.
IBU@(10mg)GQD@MOF-199 was selected for the release study due to its highest encapsulation efficiency as compared to the other composites. As it can be seen from the result, IBU@MOF-199 showed a burst of drug release and within three hours 100% of the drug was released into the simulated fluid, and according to the literature slow and controlled drug release is preferred.

To resolve the limitation of IBP@MOF-199, GQDs were inserted into the MOF-199, that increased the overall encapsulation efficiency of the polymer composite and

played its role to obtain a control drug release of 68.12% in 72 hours. To further improve the drug release and biocompatibility of the drug delivery system, chitosan a green biodegradable polymer was used to coat IBU@MOF-199, and IBP@(10mg)GQD@MOF-199. From the result obtained drug release was controlled up to 58.67 % and 50.96% respectively in the 72 hours period. These findings approve the suitability of Chitosan@IBU@GQD@MOF-199 for wound healing applications. The above **fig.5.15** compares the drug release pattern and approves an improved and controlled drug release of ibuprofen, which can be related to the special characteristics of in-situ GQDs and chitosan coating. The initial and abrupt release of ibuprofen can be due to the high concentration, but as the time passes a uniform curve is achieved. In case of GQD composite and chitosan coating the over all drug release was controlled and prolonged. This phenomenon can occur due to the hydrogen bond formation between amine and hydroxyl groups present in GQD and ibuprofen, the presence of chitosan acts as a capping agent that further increases the control release, and biocompatibility of the system, making it suitable for prolonged wound healing applications and drug delivery systems [56], [66], [84]**.**

CHAPTER 6: CONCLUSIONS AND FUTURE RECOMMENDATION

6.1   Conclusion

To conclude, in this research, the chitosan@IBP@GQD@MOF-199 system was developed with an increase encapsulation efficiency and controlled drug delivery for enhanced wound healing application system. The MOF-199 structure was made through hydrolysis in the presence of pre synthesized GQDs prepared through single step pyrolysis method followed by simple stirring at room temperature for chitosan coating. The loading of ibuprofen was confirmed through UV analysis with the help of analyzing the supernatant solution through standard beer lambert curve for ibuprofen at 264 nm absorbance wavelength. The FTIR results confirms the formation of MOF-199 by showing the standard peaks for Cu-O coordinate covalent bonding, the presence of the amine peak in GQD@MOF-199 composites successfully confirmed polymer composite formation, increase in the intensity of CH_2 peaks and shifting of O-H towards lower frequency confirmed the coating of chitosan onto the GQD@MOF-199. The XRD results clearly demonstrated the presence of characteristics planes for MOF-199 and shows no change in the observed peaks for GQD@MOF-199 composites, indicating structure of MOF-199 is still intact while composite formation, as the amorphous peaks in XRD from 18º-26º pointed towards the coating of chitosan onto MOF-199 and GQD@MOF-199.

The SEM images showed changes in the morphological structure of the composites GQD@MOF-199, the roughness at the surface of the composite increased in the presence of GQDs stating successful incorporation of GQDs onto the MOF-199 and resulting in an increase surface area which resulted in an enhanced encapsulation efficiency as compared to the MOF-199 structure. The zeta analysis showed a decrease in the overall negative charge of the system developed due to the protonation of carboxylic groups in the presence of amine functional groups as the complex polymer matrix was being synthesized.

During the release, ibuprofen at first, burst into the solution due to the high concentration but as the time passes the release rate become steady and uniform, releasing up to 43.11% of the drug in 72 hours in case of chitosan@IBP@GQD@MOF-199 due to

the formation of hydrogen bonds between amine and functional groups of GQDs and ibuprofen, and capping capability of the chitosan, making it suitable for a prolonged drug delivery system with increased encapsulation efficiency for wound healing application. However, these tests focus on in vitro drug release, in vivo studies are necessary in the future to confirm its performance with full confidence.

Overall, the research conducted establishes the fact that the synthesized chitosan@IBP@GQD@MOF-199 system can be used as drug carrier due to its high encapsulation efficiency and for controlled uniform drug delivery and prolong release of ibuprofen for wound healing applications.

6.2   Future Recommendations

However, these tests focus on in vitro drug release, in vivo studies are necessary in the future to confirm its performance, cytotoxicity, and biocompatibility with full confidence. Overall, the research conducted establishes the fact that the synthesized chitosan@IBP@GQD@MOF-199 system can be used for controlled and uniform drug delivery and prolong release of ibuprofen for wound healing applications.

REFERENCES

[1]   A. C. D. O. Gonzalez, Z. D. A. Andrade, T. F. Costa, and A. R. A. P. Medrado, "Wound healing - A literature review," *Anais Brasileiros de Dermatologia*, vol. 91, no. 5. Sociedade Brasileira de Dermatologia, pp. 614–620, Sep. 01, 2016. doi: 10.1590/abd1806-4841.20164741.

[2]   S. Hamdan *et al.*, "Nanotechnology-Driven Therapeutic Interventions in Wound Healing: Potential Uses and Applications," *ACS Cent Sci*, vol. 3, no. 3, pp. 163–175, Mar. 2017, doi: 10.1021/acscentsci.6b00371.

[3]   G. Cicco, F. Giorgino, and S. Cicco, "Wound healing in diabetes: Hemorheological and microcirculatory aspects," in *Advances in Experimental Medicine and Biology*, Springer New York LLC, 2011, pp. 263–269. doi: 10.1007/978-1-4419-7756-4_35.

[4]   E. A. Lenselink, "Role of fibronectin in normal wound healing," *Int Wound J*, vol. 12, no. 3, pp. 313–316, Jun. 2015, doi: 10.1111/iwj.12109.

[5]   N. S. Kleiman *et al.*, "Platelets: Developmental biology, physiology, and translatable platforms for preclinical investigation and drug development," *Platelets*, vol. 19, no. 4. pp. 239–251, Jun. 2008. doi: 10.1080/09537100801947442.

[6]   L. M. Morton and T. J. Phillips, "Wound healing and treating wounds Differential diagnosis and evaluation of chronic wounds," *Journal of the American Academy of Dermatology*, vol. 74, no. 4. Mosby Inc., pp. 589–605, Apr. 01, 2016. doi: 10.1016/j.jaad.2015.08.068.

[7]   M. C. Robson, D. L. Steed, and M. G. Franz, "Surgery ® Wound Healing: Biologic Features and Approaches to Maximize Healing Trajectories."

[8]   T. J. Koh and L. A. DiPietro, "Inflammation and wound healing: the role of the macrophage.," *Expert reviews in molecular medicine*, vol. 13. 2011. doi: 10.1017/S1462399411001943.

[9]   P. Rousselle, M. Montmasson, and C. Garnier, "Extracellular matrix contribution to skin wound re-epithelialization," *Matrix Biology*, vol. 75–76. Elsevier B.V., pp. 12–26, Jan. 01, 2019. doi: 10.1016/j.matbio.2018.01.002.

[10]   P. Krzyszczyk, R. Schloss, A. Palmer, and F. Berthiaume, "The role of macrophages in acute and chronic wound healing and interventions to promote pro-wound healing phenotypes," *Frontiers in Physiology*, vol. 9, no. MAY. Frontiers Media S.A., May 01, 2018. doi: 10.3389/fphys.2018.00419.

[11]   K. S. Midwood, L. V. Williams, and J. E. Schwarzbauer, "Tissue repair and the dynamics of the extracellular matrix," *International Journal of Biochemistry and Cell Biology*, vol. 36, no. 6. Elsevier Ltd, pp. 1031–1037, 2004. doi: 10.1016/j.biocel.2003.12.003.

[12]   J. Li, Y. P. Zhang, and R. S. Kirsner, "Angiogenesis in wound repair: Angiogenic growth factors and the extracellular matrix," *Microscopy Research and Technique*, vol. 60, no. 1. Wiley-Liss Inc., pp. 107–114, Jan. 01, 2003. doi: 10.1002/jemt.10249.

[13]   Y. Xiao *et al.*, "Diabetic wound regeneration using peptide-modified hydrogels to target re-epithelialization," *Proc Natl Acad Sci U S A*, vol. 113, no. 40, pp. E5792–E5801, Oct. 2016, doi: 10.1073/pnas.1612277113.

[14]   S. Chen, J. Lu, T. You, and D. Sun, "Metal-organic frameworks for improving wound healing," *Coordination Chemistry Reviews*, vol. 439. Elsevier B.V., Jul. 15, 2021. doi: 10.1016/j.ccr.2021.213929.

[15]   P. Olczyk, Ł. Mencner, and K. Komosinska-Vassev, "The role of the extracellular matrix components in cutaneous wound healing," *BioMed Research International*, vol. 2014. Hindawi Publishing Corporation, 2014. doi: 10.1155/2014/747584.

[16]   R. F. Pereira and P. J. Bártolo, "Traditional Therapies for Skin Wound Healing," *Advances in Wound Care*, vol. 5, no. 5. Mary Ann Liebert Inc., pp. 208–229, May 01, 2016. doi: 10.1089/wound.2013.0506.

[17]   L. Vandamme, A. Heyneman, H. Hoeksema, J. Verbelen, and S. Monstrey, "Honey in modern wound care: A systematic review," *Burns*, vol. 39, no. 8. pp. 1514–1525, Dec. 2013. doi: 10.1016/j.burns.2013.06.014.

[18]   R. Tiwari and K. Pathak, "Local Drug Delivery Strategies towards Wound Healing," *Pharmaceutics*, vol. 15, no. 2. MDPI, Feb. 01, 2023. doi: 10.3390/pharmaceutics15020634.

[19]   O. Givol, R. Kornhaber, D. Visentin, M. Cleary, J. Haik, and M. Harats, "A systematic review of Calendula officinalis extract for wound healing," *Wound Repair and Regeneration*, vol. 27, no. 5. Blackwell Publishing Inc., pp. 548–561, Sep. 01, 2019. doi: 10.1111/wrr.12737.

[20]   R. G. Frykberg and J. Banks, "Challenges in the Treatment of Chronic Wounds," *Adv Wound Care (New Rochelle)*, vol. 4, no. 9, pp. 560–582, Sep. 2015, doi: 10.1089/wound.2015.0635.

[21]   K. T. B. Santema *et al.*, "Hyperbaric oxygen therapy in the treatment of ischemic lower-extremity ulcers in patients with diabetes: Results of the DAMO2CLES multicenter randomized clinical trial," *Diabetes Care*, vol. 41, no. 1, pp. 112–119, Jan. 2018, doi: 10.2337/dc17-0654.

[22]   D. Zhu and Q. Qian, "Optimal switching time control of the hyperbaric oxygen therapy for a chronic wound," *Mathematical Biosciences and Engineering*, vol. 16, no. 6, pp. 8290–8308, 2019, doi: 10.3934/mbe.2019419.

[23]   W. Cai, J. Wang, C. Chu, W. Chen, C. Wu, and G. Liu, "Metal–Organic Framework-Based Stimuli-Responsive Systems for Drug Delivery," *Advanced Science*, vol. 6, no. 1. John Wiley and Sons Inc., Jan. 09, 2019. doi: 10.1002/advs.201801526.

[24]   K. Hola, Y. Zhang, Y. Wang, E. P. Giannelis, R. Zboril, and A. L. Rogach, "Carbon dots - Emerging light emitters for bioimaging, cancer therapy and optoelectronics," *Nano Today*, vol. 9, no. 5. Elsevier B.V., pp. 590–603, 2014. doi: 10.1016/j.nantod.2014.09.004.

[25]   Y. Wang and A. Hu, "Carbon quantum dots: Synthesis, properties and applications," *J Mater Chem C Mater*, vol. 2, no. 34, pp. 6921–6939, Sep. 2014, doi: 10.1039/c4tc00988f.

[26]   X. Xu *et al.*, "Electrophoretic analysis and purification of fluorescent single-walled carbon nanotube fragments," *J Am Chem Soc*, vol. 126, no. 40, pp. 12736–12737, Oct. 2004, doi: 10.1021/ja040082h.

[27]   J. A. Jaleel and K. Pramod, "Artful and multifaceted applications of carbon dot in biomedicine," *Journal of Controlled Release*, vol. 269. Elsevier B.V., pp. 302–321, Jan. 10, 2018. doi: 10.1016/j.jconrel.2017.11.027.

[28]   M. L. Liu, B. Bin Chen, C. M. Li, and C. Z. Huang, "Carbon dots: Synthesis, formation mechanism, fluorescence origin and sensing applications," *Green Chemistry*, vol. 21, no. 3. Royal Society of Chemistry, pp. 449–471, 2019. doi: 10.1039/c8gc02736f.

[29]   P. G. Luo *et al.*, "Carbon 'quantum' dots for optical bioimaging," *J Mater Chem B*, vol. 1, no. 16, pp. 2116–2127, Apr. 2013, doi: 10.1039/c3tb00018d.

[30]   P. Yi, X. Xu, B. Qiu, and H. Li, "Impact of chitosan membrane culture on the expression of pro- and anti-inflammatory cytokines in mesenchymal stem cells," *Exp Ther Med*, Aug. 2020, doi: 10.3892/etm.2020.9108.

[31]   A. A. Wardana, A. Koga, F. Tanaka, and F. Tanaka, "Antifungal features and properties of chitosan/sandalwood oil Pickering emulsion coating stabilized by appropriate cellulose nanofiber dosage for fresh fruit application," *Sci Rep*, vol. 11, no. 1, Dec. 2021, doi: 10.1038/s41598-021-98074-w.

[32]   C. Ardean *et al.*, "Factors influencing the antibacterial activity of chitosan and chitosan modified by functionalization," *International Journal of Molecular Sciences*, vol. 22, no. 14. MDPI AG, Jul. 02, 2021. doi: 10.3390/ijms22147449.

[33]   C. Lin *et al.*, "Carbon dots embedded metal organic framework @ chitosan core-shell nanoparticles for vitro dual mode imaging and pH-responsive drug delivery,"

Microporous and Mesoporous Materials, vol. 293, Feb. 2020, doi: 10.1016/j.micromeso.2019.109775.

[34] K. S. Asha, R. Bhattacharjee, and S. Mandal, "Complete Transmetalation in a Metal–Organic Framework by Metal Ion Metathesis in a Single Crystal for Selective Sensing of Phosphate Ions in Aqueous Media," *Angewandte Chemie*, vol. 128, no. 38, pp. 11700–11704, Sep. 2016, doi: 10.1002/ange.201606185.

[35] J. A. Mason *et al.*, "Methane storage in flexible metal-organic frameworks with intrinsic thermal management," *Nature*, vol. 527, no. 7578, pp. 357–361, Nov. 2015, doi: 10.1038/nature15732.

[36] S. Zheng *et al.*, "Transition-Metal (Fe, Co, Ni) Based Metal-Organic Frameworks for Electrochemical Energy Storage," *Advanced Energy Materials*, vol. 7, no. 18. Wiley-VCH Verlag, Sep. 20, 2017. doi: 10.1002/aenm.201602733.

[37] J. D. Sosa, T. F. Bennett, K. J. Nelms, B. M. Liu, R. C. Tovar, and Y. Liu, "Metal–organic framework hybrid materials and their applications," *Crystals*, vol. 8, no. 8. MDPI AG, Aug. 14, 2018. doi: 10.3390/cryst8080325.

[38] S. Wuttke, M. Lismont, A. Escudero, B. Rungtaweevoranit, and W. J. Parak, "Positioning metal-organic framework nanoparticles within the context of drug delivery – A comparison with mesoporous silica nanoparticles and dendrimers," *Biomaterials*, vol. 123, pp. 172–183, Apr. 2017, doi: 10.1016/j.biomaterials.2017.01.025.

[39] M. Lismont, L. Dreesen, and S. Wuttke, "Metal-Organic Framework Nanoparticles in Photodynamic Therapy: Current Status and Perspectives," *Advanced Functional Materials*, vol. 27, no. 14. Wiley-VCH Verlag, Apr. 11, 2017. doi: 10.1002/adfm.201606314.

[40] H. Wang *et al.*, "Enzymatic Inverse Opal Hydrogel Particles for Biocatalyst," *ACS Appl Mater Interfaces*, vol. 9, no. 15, pp. 12914–12918, Apr. 2017, doi: 10.1021/acsami.7b01866.

[41] H. Furukawa, K. E. Cordova, M. O'Keeffe, and O. M. Yaghi, "The chemistry and applications of metal-organic frameworks," *Science*, vol. 341, no. 6149. American Association for the Advancement of Science, 2013. doi: 10.1126/science.1230444.

[42] Z. Rao, K. Feng, B. Tang, and P. Wu, "Surface decoration of amino-functionalized metal-organic framework/graphene oxide composite onto polydopamine-coated membrane substrate for highly efficient heavy metal removal," *ACS Appl Mater Interfaces*, vol. 9, no. 3, pp. 2594–2605, Jan. 2017, doi: 10.1021/acsami.6b15873.

[43] Z. Rao, K. Feng, B. Tang, and P. Wu, "Construction of well interconnected metal-organic framework structure for effectively promoting proton conductivity of proton exchange membrane," *J Memb Sci*, vol. 533, pp. 160–170, 2017, doi: 10.1016/j.memsci.2017.03.031.

[44] W. Cai, C. C. Chu, G. Liu, and Y. X. J. Wáng, "Metal-Organic Framework-Based Nanomedicine Platforms for Drug Delivery and Molecular Imaging," *Small*, vol. 11, no. 37. Wiley-VCH Verlag, pp. 4806–4822, Oct. 01, 2015. doi: 10.1002/smll.201500802.

[45] W. Xuan, C. Zhu, Y. Liu, and Y. Cui, "Mesoporous metal–organic framework materials," *Chem Soc Rev*, vol. 41, no. 5, pp. 1677–1695, Feb. 2012, doi: 10.1039/c1cs15196g.

[46] L. L. Tan *et al.*, "Zn2+-Triggered Drug Release from Biocompatible Zirconium MOFs Equipped with Supramolecular Gates," *Small*, vol. 11, no. 31, pp. 3807–3813, Aug. 2015, doi: 10.1002/smll.201500155.

[47] K. M. L. Taylor-Pashow, J. Della Rocca, Z. Xie, S. Tran, and W. Lin, "Postsynthetic modifications of iron-carboxylate nanoscale metal-organic frameworks for imaging and drug delivery," *J Am Chem Soc*, vol. 131, no. 40, pp. 14261–14263, Oct. 2009, doi: 10.1021/ja906198y.

[48] N. R. Dhumal, M. P. Singh, J. A. Anderson, J. Kiefer, and H. J. Kim, "Molecular Interactions of a Cu-Based Metal-Organic Framework with a Confined

Imidazolium-Based Ionic Liquid: A Combined Density Functional Theory and Experimental Vibrational Spectroscopy Study," *Journal of Physical Chemistry C*, vol. 120, no. 6, pp. 3295–3304, Feb. 2016, doi: 10.1021/acs.jpcc.5b10123.

[49]   J. A. Mason, M. Veenstra, and J. R. Long, "Evaluating metal-organic frameworks for natural gas storage," *Chemical Science*, vol. 5, no. 1. pp. 32–51, Jan. 2014. doi: 10.1039/c3sc52633j.

[50]   A. C. McKinlay *et al.*, "BioMOFs: Metal-organic frameworks for biological and medical applications," *Angewandte Chemie - International Edition*, vol. 49, no. 36. pp. 6260–6266, Aug. 23, 2010. doi: 10.1002/anie.201000048.

[51]   X. Li *et al.*, "New insights into the degradation mechanism of metal-organic frameworks drug carriers," *Sci Rep*, vol. 7, no. 1, Dec. 2017, doi: 10.1038/s41598-017-13323-1.

[52]   J. Xiao *et al.*, "Copper Metal-Organic Framework Nanoparticles Stabilized with Folic Acid Improve Wound Healing in Diabetes," *ACS Nano*, vol. 12, no. 2, pp. 1023–1032, Feb. 2018, doi: 10.1021/acsnano.7b01850.

[53]   B. Supronowicz, A. Mavrandonakis, and T. Heine, "Interaction of biologically important organic molecules with the unsaturated copper centers of the HKUST-1 metal-organic framework: An ab-initio study," *Journal of Physical Chemistry C*, vol. 119, no. 6, pp. 3024–3032, Feb. 2015, doi: 10.1021/jp507144w.

[54]   C. Chiericatti, J. C. Basilico, M. L. Zapata Basilico, and J. M. Zamaro, "Novel application of HKUST-1 metal-organic framework as antifungal: Biological tests and physicochemical characterizations," *Microporous and Mesoporous Materials*, vol. 162, pp. 60–63, Nov. 2012, doi: 10.1016/j.micromeso.2012.06.012.

[55]   A. C. McKinlay *et al.*, "Multirate delivery of multiple therapeutic agents from metal-organic frameworks," *APL Mater*, vol. 2, no. 12, Dec. 2014, doi: 10.1063/1.4903290.

[56] M. Pooresmaeil, Y. Hassanpouraghdam, and H. Namazi, "Chitosan/carboxymethyl starch bio-coated naproxen@GQDs/Copper glutamate MOFs: A new system for colon-specific drug delivery relay on the special structure of the used polymers," *Eur Polym J*, vol. 184, Feb. 2023, doi: 10.1016/j.eurpolymj.2022.111802.

[57] M. Zhang *et al.*, "Ag@MOF-loaded chitosan nanoparticle and polyvinyl alcohol/sodium alginate/chitosan bilayer dressing for wound healing applications," *Int J Biol Macromol*, vol. 175, pp. 481–494, Apr. 2021, doi: 10.1016/j.ijbiomac.2021.02.045.

[58] Y. Hassanpouraghdam, M. Pooresmaeil, and H. Namazi, "In-vitro evaluation of the 5-fluorouracil loaded GQDs@Bio-MOF capped with starch biopolymer for improved colon-specific delivery," *Int J Biol Macromol*, vol. 221, pp. 256–267, Nov. 2022, doi: 10.1016/j.ijbiomac.2022.08.167.

[59] S. Javanbakht, P. Nezhad-Mokhtari, A. Shaabani, N. Arsalani, and M. Ghorbani, "Incorporating Cu-based metal-organic framework/drug nanohybrids into gelatin microsphere for ibuprofen oral delivery," *Materials Science and Engineering C*, vol. 96, pp. 302–309, Mar. 2019, doi: 10.1016/j.msec.2018.11.028.

[60] C. Lin *et al.*, "Carbon dots embedded metal organic framework @ chitosan core-shell nanoparticles for vitro dual mode imaging and pH-responsive drug delivery," *Microporous and Mesoporous Materials*, vol. 293, Feb. 2020, doi: 10.1016/j.micromeso.2019.109775.

[61] P. I. Morgado, S. P. Miguel, I. J. Correia, and A. Aguiar-Ricardo, "Ibuprofen loaded PVA/chitosan membranes: A highly efficient strategy towards an improved skin wound healing," *Carbohydr Polym*, vol. 159, pp. 136–145, Mar. 2017, doi: 10.1016/j.carbpol.2016.12.029.

[62] R. D. Pavaloiu, A. Stoica-Guzun, M. Stroescu, S. I. Jinga, and T. Dobre, "Composite films of poly(vinyl alcohol)-chitosan-bacterial cellulose for drug controlled release," *Int J Biol Macromol*, vol. 68, pp. 117–124, 2014, doi: 10.1016/j.ijbiomac.2014.04.040.

[63]   A. Nisar, M. A. Khan, and Z. Hussain, "Synthesis and characterization of PANI/MOF-199/Ag nanocomposite and its potential application as non-enzymatic electrochemical sensing of dopamine," *Journal of the Korean Ceramic Society*, vol. 59, no. 3, pp. 359–369, May 2022, doi: 10.1007/s43207-021-00166-w.

[64]   Y. Cui, W. Duan, Y. Jin, F. Wo, F. Xi, and J. Wu, "Graphene quantum dot-decorated luminescent porous silicon dressing for theranostics of diabetic wounds," *Acta Biomater*, vol. 131, pp. 544–554, Sep. 2021, doi: 10.1016/j.actbio.2021.07.018.

[65]   D. Mukherjee, P. Das, S. Kundu, L. Mohan Kundu, and B. Mandal, "Graphene quantum dots decorated MIL-100(Fe) composites for dye degradation," *J Photochem Photobiol A Chem*, vol. 442, Aug. 2023, doi: 10.1016/j.jphotochem.2023.114776.

[66]   E. G. Lemraski, S. Alibeigi, and Z. Abbasi, "Ibuprofen@silver loaded on poly(vinyl alcohol)/chitosan co-polymer scaffold as a novel drug delivery system," *Mater Today Commun*, vol. 33, Dec. 2022, doi: 10.1016/j.mtcomm.2022.104311.

[67]   I. Ghaffar *et al.*, "Synthesis of chitosan coated metal organic frameworks (MOFs) for increasing vancomycin bactericidal potentials against resistant S. aureus strain," *Materials Science and Engineering C*, vol. 105, Dec. 2019, doi: 10.1016/j.msec.2019.110111.

[68]   S. Yoosefi *et al.*, "Dual drug delivery system based on layered double hydroxides/carboxymethyl cellulose-poly ethylene oxide bionanocomposite electrospun fibrous mats: Fabrication, characterization, in-vitro and in-vivo studies," *Int J Biol Macromol*, vol. 222, pp. 3142–3154, Dec. 2022, doi: 10.1016/j.ijbiomac.2022.10.087.

[69]   Z. Liu *et al.*, "Size effect of graphene quantum dots on photoluminescence," *Molecules*, vol. 26, no. 13, Jul. 2021, doi: 10.3390/molecules26133922.

[70] L. Wang *et al.*, "Gram-scale synthesis of single-crystalline graphene quantum dots with superior optical properties," *Nat Commun*, vol. 5, 2014, doi: 10.1038/ncomms6357.

[71] X. Wu, F. Tian, W. Wang, J. Chen, M. Wu, and J. X. Zhao, "Fabrication of highly fluorescent graphene quantum dots using L-glutamic acid for in vitro/in vivo imaging and sensing," *J Mater Chem C Mater*, vol. 1, no. 31, pp. 4676–4684, Jul. 2013, doi: 10.1039/c3tc30820k.

[72] Z. Ansari-Asl, Z. Shahvali, R. Sacourbaravi, E. Hoveizi, and E. Darabpour, "Cu(II) metal-organic framework@Polydimethylsiloxane nanocomposite sponges coated by chitosan for antibacterial and tissue engineering applications," *Microporous and Mesoporous Materials*, vol. 336, May 2022, doi: 10.1016/j.micromeso.2022.111866.

[73] X. Dai *et al.*, "Direct z-scheme ZnCo2S4/MOF-199 constructed by bimetallic sulfide modified MOF for photocatalytic hydrogen evolution," *Appl Surf Sci*, vol. 639, Dec. 2023, doi: 10.1016/j.apsusc.2023.158142.

[74] Y. Wang *et al.*, "Effect of hierarchical porous MOF-199 regulated by PVP on their ambient desulfurization performance," *Fuel*, vol. 319, Jul. 2022, doi: 10.1016/j.fuel.2022.123845.

[75] Y. Cao, G. Wang, H. Liu, Y. Li, Z. Jin, and Q. Ma, "Regular octahedron Cu-MOFs modifies Mn0.05Cd0.95S nanoparticles to form a S-scheme heterojunction for photocatalytic hydrogen evolution," *Int J Hydrogen Energy*, vol. 46, no. 10, pp. 7230–7240, Feb. 2021, doi: 10.1016/j.ijhydene.2020.11.214.

[76] G. A. Bodkhe *et al.*, "Ag@MOF-199 metal organic framework for selective detection of nickel ions in aqueous media," *Ceram Int*, vol. 49, no. 4, pp. 6772–6779, Feb. 2023, doi: 10.1016/j.ceramint.2022.10.135.

[77] S. Tajik *et al.*, "Carbon and graphene quantum dots: A review on syntheses, characterization, biological and sensing applications for neurotransmitter

determination," *RSC Advances*, vol. 10, no. 26. Royal Society of Chemistry, pp. 15406–15429, Apr. 20, 2020. doi: 10.1039/d0ra00799d.

[78] Y. Chen, B. Y. Zhai, Y. N. Liang, and Y. Li, "Hybrid photocatalysts using semiconductor/MOF/graphene oxide for superior photodegradation of organic pollutants under visible light," *Mater Sci Semicond Process*, vol. 107, Mar. 2020, doi: 10.1016/j.mssp.2019.104838.

[79] G. A. Bodkhe *et al.*, "Ag@MOF-199 metal organic framework for selective detection of nickel ions in aqueous media," *Ceram Int*, vol. 49, no. 4, pp. 6772–6779, Feb. 2023, doi: 10.1016/j.ceramint.2022.10.135.

[80] M. Roushani, M. Mavaei, and H. R. Rajabi, "Graphene quantum dots as novel and green nano-materials for the visible-light-driven photocatalytic degradation of cationic dye," *J Mol Catal A Chem*, vol. 409, pp. 102–109, Aug. 2015, doi: 10.1016/j.molcata.2015.08.011.

[81] P. He *et al.*, "Processable aqueous dispersions of graphene stabilized by graphene quantum dots," *Chemistry of Materials*, vol. 27, no. 1, pp. 218–226, Jan. 2015, doi: 10.1021/cm503782p.

[82] A. H. Shah *et al.*, "Adsorption kinetics of simulated mixture wastewaters over porous Bi2MoO6@BiOCl@MOF-199 heterostructure," *J Solid State Chem*, vol. 307, Mar. 2022, doi: 10.1016/j.jssc.2021.122835.

[83] W. Liu and X. Zhu, "A novel fluorescence 'turn off-on' sensor based on N-doped graphene quantum dots in amino acid ionic liquid medium and its application," *Talanta*, vol. 197, pp. 59–67, May 2019, doi: 10.1016/j.talanta.2019.01.008.

[84] L. Dian *et al.*, "Cubic phase nanoparticles for sustained release of ibuprofen: Formulation, characterization, and enhanced bioavailability study," *Int J Nanomedicine*, vol. 8, pp. 845–854, Feb. 2013, doi: 10.2147/IJN.S40547.